A SEARCH FOR W_R AND HEAVY MAJORANA NEUTRINO IN DIMUON CHANNEL WITH THE ATLAS EXPERIMENT

by

Reza Yoosoofmiya

BSc in Physics, University of Colombo, Sri Lanka, 2003

MSc in Physics, University of Pittsburgh, USA, 2006

Submitted to the Graduate Faculty of

the Department of Physics and Astronomy in partial fulfillment

of the requirements for the degree of

Doctor of Philosophy

University of Pittsburgh

2013

UNIVERSITY OF PITTSBURGH

DEPARTMENT OF PHYSICS AND ASTRONOMY

This dissertation was presented

by

Reza Yoosoofmiya

It was defended on

April 15th 2013

and approved by

Dr. Vladimir Savinov, Associate Professor, Department of Physics and Astronomy

Dr. Roy Briere, Professor, Department of Physics, CMU

Dr. Steve Dytman, Professor, Department of Physics and Astronomy

Dr. Arthur Kosowsky, Professor, Department of Physics and Astronomy

Dr. Vittorio Paolone, Associate Professor, Department of Physics and Astronomy

Dissertation Director: Dr. Vladimir Savinov, Associate Professor, Department of Physics and Astronomy

A SEARCH FOR W_R AND HEAVY MAJORANA NEUTRINO IN DIMUON CHANNEL WITH THE ATLAS EXPERIMENT

Reza Yoosoofmiya, PhD

University of Pittsburgh, 2013

This thesis describes a search for hypothetical heavy neutrinos, N, and right-handed gauge bosons, W_R, in events with two high transverse momentum muons and at least one high transverse momentum hadronic jet. The results were obtained from data corresponding to an integrated luminosity of 4.7 fb^{-1} collected in proton-proton collisions at $\sqrt{s}$ =7 TeV with the ATLAS detector at the CERN Large Hadron Collider. No excess above the Standard Model background expectation is observed. Excluded mass regions for Majorana neutrinos are presented in the framework of Left-Right Symmetric Model which introduces interactions that violate lepton and lepton-flavor numbers. The results described in this thesis represent limits on the masses of heavy neutrinos and W_R bosons obtained in direct searches.

TABLE OF CONTENTS

LIST OF TABLES

LIST OF FIGURES

1.0 INTRODUCTION

1.1 FRAMEWORK OF PARTICLE PHYSICS

1.1.1 Standard Model of Particle Physics

Forces observed in nature can be classified into four fundamental categories according to present-day understanding of their manifestations and strengths. These four fundamental forces listed in order of increasing strength are: Gravitation, Weak, Electromagnetic and Strong. The latter three forces have been modeled to a great accuracy within the paradigm of quantum field theory. The collective description of the three forces and their interplay with the matter is known as the Standard Model of particle physics (SM). The framework of the Standard Model is a quantum field theory (QFT), which is a result of unifying quantum mechanics and special relativity. The main driving principles behind QFT are local gauge symmetry and Lorentz invariance. The group-theoretical structure of the SM is $SU(3)_c \times SU(2)_L \times U(1)_Y$.

The SM can be partly described in terms of its particle content, by classifying the fundamental particles into two categories, matter particles and force carriers. The matter particles include quarks and leptons. Force carriers include vector gauge bosons γ, Z, $W^{\pm}$ and colored gluons. A summary of the SM particles is shown in Fig. 1.

The SM has been very successful in describing the fundamental interactions. The confirmation of its predictions by discoveries of bottom and top quarks, tau neutrino and the Higgs boson have further bolstered its central role in particle physics. However, despite enormous success, SM stands incomplete for a variety of reasons.

The Standard Model does not incorporate one of the 4 fundamental forces, gravity.

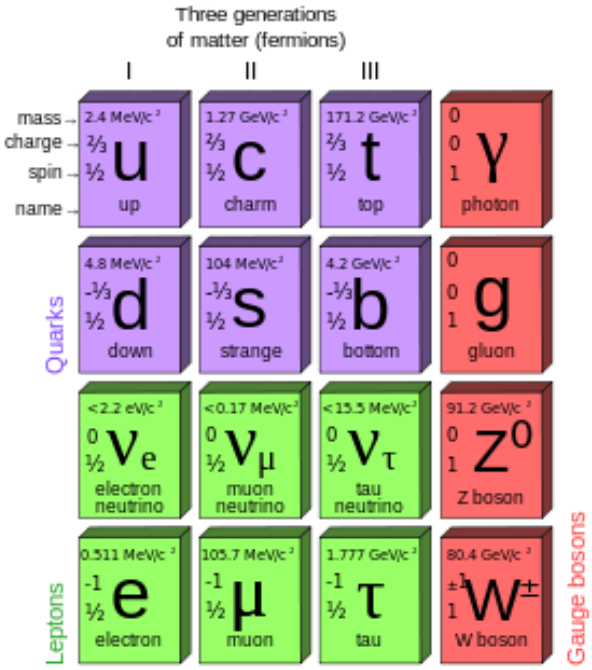

Figure 1: Particles of the SM.

Also, the SM does not have an explanation for the baryon asymmetry, dark matter or the dark energy. The SM does not account for the non-zero mass of at least some of the known neutrinos, which has been established by the observation of neutrino oscillation [1, 2]. Although a Dirac mass term for the neutrino could be added, the smallness of the mass is difficult to explain (the observed neutrino masses are several orders of magnitude smaller than the next lightest SM elementary particle, electron). Furthermore, the SM suffers from the so-called fine tuning problem, as some of its parameters need precise adjustments in order to agree with the measured values. There are 19 parameters in the SM, which is deemed to be inelegant. In addition, the particles come in three generations, which the SM does not explain either. Last but not the least is the explanation of conservation of baryon, lepton and lepton flavor numbers. In the framework of the SM the conservation of these quantum numbers is "accidental", *i.e.* is not associated with any fundamental gauge symmetry. This is quite puzzling, because in absence of a gauge symmetry "protecting"

these quantum numbers, each of the corresponding symmetries would be violated. In case of baryon (B) and lepton (L) numbers this requires some completely new theoretical approach to the baryogenesis, where it is usually assumed that $B - L$ is conserved because of some gauge symmetry we have not yet found a confirmation for.

1.1.2 Left-Right Symmetric Model and Heavy Neutrino

While the SM of particle physics describes relatively low-energy interactions remarkably well, the limitations of the SM suggest it is just an approximation of a more complete theory. A popular candidate for such a theory is supersymmetry (often abbreviated to SUSY). Supersymmetry is a set of extension of the Poincare symmetry that the Standard Model is based on, which implies the existence of partners of all known SM particles. The partner particles ("sparticles") have spin differing by 1/2 to that of the SM particles: partners of bosons are fermions, and vice versa. [3, 4, 5]

Though Left-Right Symmetric Model (LRSM) does not extend SM gauge symmetries to the extent of SUSY (which has not been confirmed by the LHC at the EWSB energy scale, making it less relevant for the energy scale explored in this work), LRSM offers an elegant solution to the neutrino mass problem while restoring parity in the SM Lagrangian. While SUSY does not seem to realize at EWSB energy scale, it is worth to note that the LRSM ideas could be easily incorporated in a SUSY extension of the SM.

The first implementations of LRSM were developed by J.C. Pati and A. Salam [6], and R.N. Mohapatra and J.C. Pati [7]. Left-Right Symmetry (LRS) is a GUT-inspired extension of the SM Lagrangian to a gauge symmetry of higher order represented by $SU(3)_C \times SU(2)_L \times SU(2)_R \times U(1)_{B-L}$, where left and right chiral fields are treated equally. The gauge invariant Lagrangian for the quarks and leptons leads to the following gauge boson interactions with fermions:

$$\begin{aligned}\mathcal{L}_{gauge} = & g_L \left[\bar{q}_L \gamma_\mu \frac{\tau}{2} q_L + \bar{\psi}_L \gamma_\mu \frac{\tau}{2} \psi_L\right] \cdot W_L^\mu \\ & + g_R \left[\bar{q}_R \gamma_\mu \frac{\tau}{2} q_R + \bar{\psi}_R \gamma_\mu \frac{\tau}{2} \psi_R\right] \cdot W_R^\mu \\ & + g\prime \left[\frac{1}{6} \bar{q} \gamma_\mu q - \frac{1}{2} \bar{\psi} \gamma_\mu \psi\right] B^\mu,\end{aligned} \tag{1.1}$$

where W_L^μ, W_R^μ and B^μ are the gauge bosons corresponding to the groups $SU(2)_L$, $SU(2)_R$ and $U(1)_{B-L}$, respectively, whereas g_L, g_R and g' are the corresponding gauge coupling constants.

The $B - L$ corresponds to the conserved difference between baryon and lepton quantum numbers which is an accidental symmetry of the SM, but is generally expected to be a quantum number of some BSM gauge symmetry at very high energies, where this symmetry is necessary in many models of the baryogenesis. Left-right symmetric treatment of weak interaction requires all left-handed fermions to have right-handed partners, therefore three new neutral fermions are introduced: the right-handed neutrinos, that are often denoted ν_R or, to emphasize their heavy masses, N_R. At higher energies, above the EWS and LRS breaking energy scales, where the symmetries are exact, parity is conserved. Models based on LRS ideas address several important topics that are briefly discussed below: nonzero masses of the three known light neutrinos via the seesaw mechanism, SUSY interpretation of dark matter via lightest supersymmetric particle (LSP), and baryogenesis via leptogenesis. [8] [9] [10] In general, accounting for neutrino masses in a fully renormalizable way (by extending the SM Lagrangian) requires introducing some higher-order gauge symmetries and higher-rank multiplets that include old and new fermions. Of course, if such symmetries are broken at extremely high energies (and the new particles are enormously heavy), one could use the formalism of effective field theories, where the effects of the BSM physics are accounted for by various operators and BSM mass scales in the perturbative expansion of Wilson coefficients. This breaks the renormalizability of the studied model but has become an acceptable theoretical practice.

A particularly interesting mass generation mechanism for the known neutrinos involves the three new right-handed neutrino fields and a triplet of Higgs fields that gives rise to doubly-charged physical Higgses. [11, 12] This is the mechanism implemented in the LRSM that we use as a theoretical guide in our studies. Such LRS breaking allows to explain the masses of neutrinos via the seesaw mechanism [13, 14, 15, 16] and the quantization of electric charge (this is another important physical property that the SM does not explain).

The mass terms of the Lagrangian for the neutrino sector can be written in the matrix

form as in 1.2 [14].

$$\mathcal{L}^{\nu}_{mass} = \left(\nu^T N^T\right) \mathcal{M} \begin{pmatrix} \nu \\ N \end{pmatrix} + h.c, \tag{1.2}$$

where

$$\mathcal{M} = \begin{pmatrix} 0 & h_1\kappa \\ h_1\kappa & h_3 v \end{pmatrix} \tag{1.3}$$

ν and N represents the fields of the neutrinos. In the mass matrix $\mathcal{M}$, h_1 and h_3 are Yukawa coupling strengths, while κ and v are the vacuum expectation values of new Higgs field, introduced in LRSM.

Diagonalization [13] of the mass matrix given in Equation 1.3 gives rise to the seesaw mechanism. In the seesaw mechanism the masses of the light neutrinos are directly proportional to the squared Dirac mass ($m_D = h_1\kappa$) (that are expected to be non-zero for all fermions) and inversely proportional to the masses of the new heavy neutrinos (M): $m_\nu \approx m_D^2/M_N$. The name "seesaw" is derived from the inverse relationship between the masses of the heavy neutrino and the light neutrino. The seesaw mechanism mixes right-handed and left-handed neutrinos, therefore making them all Majorana particles (i.e., their own antiparticles because eigenstates of the diagonalized matrix are eigenstates of charge conjugation operator and are linear combinations of the eigenstates before diagonalization). Generally speaking, a Lagrangian is written for massless quantum fields, not for physical particles. Particles we observe acquire masses when some of the symmetries of the Lagrangian are spontaneously broken. One can choose a symmetry breaking scenario, where the Lagrangian would contain the Majorana mass terms for the new right-handed neutrino fields and the Dirac mass terms for the known left-handed neutrino fields. In such case physical particles, *i.e.* the neutrinos we observe would be of Majorana nature via the neutrino mass matrix diagonalization. Note that Majorana neutrinos would explain also neutrinoless double-beta decay ($0\nu\beta\beta$).

Majorana neutrinos violate lepton number (L) conservation which is an accidental, *i.e.*, of non-gauge origin, symmetry of the SM. This symmetry, along with other accidental symmetries of SM, such as conservation of baryon number B and the three lepton flavor numbers

are expected to be violated at very high energies. However, most theoretically sound explanations [8, 9, 10] of baryogenesis, *i.e.*, asymmetry between matter and antimatter in visible universe, require conservation of $B-L$, the difference between baryon and lepton numbers. Such conservation law, according to today's theoretical point of view, requires $B-L$ to be a gauge symmetry (because all non-gauge symmetries are violated at very high energies). Lepton number violation due to Majorana neutrinos could be easily reconciled with the required condition for baryogenesis in the framework of LRS, where each of the quantum numbers B and L is violated, however, $B-L$ is "protected", as it is associated with gauge symmetry of the theory. Therefore LRS and Majorana neutrinos provide very elegant solution of the baryogenesis via leptogenesis, where non-conservation of L is compensated by non-conservation of B, therefore allowing violation of lepton number to appear as the asymmetry between matter and antimatter, *i.e.*, violation of baryon number. Baryon number violation is one of the three Sakharov's conditions [10] for baryogenesis. The other two conditions, namely sufficient amount of CP violation and departure from thermal equilibrium could be easily satisfied by CP violation in neutrino sector (including heavy neutrinos via their own PNMS matrix [17]) and the expansion of the universe, respectively.

To accomplish the baryogenesis, in leptogenesis L is violated in decays of heavy neutrinos, and then the excess of L is transferred into the excess of B via a non-perturbative (*i.e.* there is no Feynman diagram describing such interaction in perturbation theory) process that involves the so-called Sphalerons [18]. According to theoretical predictions, the asymmetry between matter and antimatter created in such transitions would be washed away when the universe starts cooling down, unless $B-L$ is conserved, which is a part of LRS by design. In addition to new Higgses and heavy Majorana neutrinos, LRSMs introduce new intermediate vector bosons W_R and Z' and left-right mixing parameter.

Current constraints on the masses of N_R, W_R and Z' come from variety of sources. Heavy neutrinos were previously searched for at LEP and excluded for masses up to ≈ 100 GeV [19, 20, 21, 22]. The most restrictive, preLHC limit on W_R mass comes from $K_L - K_S$ mass difference, which puts the lower limit on W_R mass at 1.6 TeV. [23] Best directly-measured, pre LHC mass limit on the W_R comes from the Tevatron experiments where they put the upper limit of W_R mass at 720 GeV at 95% C.L. [24, 25]. The first paper [26]

published by our group excludes W_R mass up to 1 TeV. Most recent paper published by our ATLAS group in March 2012 using 2.1 fb^{-1} of data puts the lower limit on W_R mass at 1.8 TeV [27].

Production of the new intermediate vector bosons W_R and Z' at the LHC would be due to the same processes as for the standard W and Z, while their decays would be the source of the new heavy Majorana neutrinos (See Fig. 2). However, due to the Majorana nature of the heavy neutrino, it can decay into a lepton of either charge. This allows for a unique nonSM signal signature, where the final state two leptons can be of the same sign.

The analysis described in this thesis looks for same-sign as well as opposite-sign final state dimuons. Same-sign dimuons are a very important signature of Majorana neutrinos, which, being their own anti-particles, could decay to a lepton of either charge. The background contribution to same-sign dileptons is much smaller than to opposite-sign dileptons.

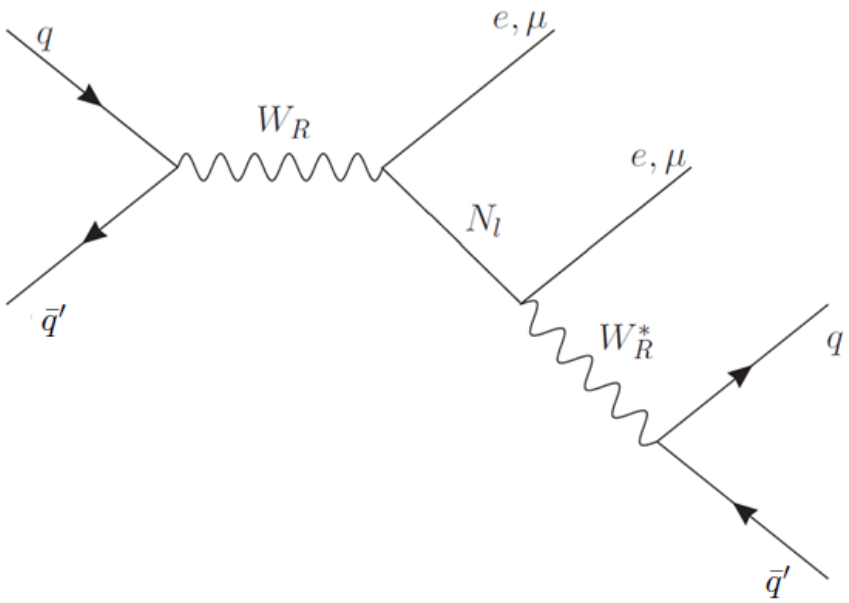

Figure 2: Feynman diagram for the production of right-handed W_R boson.

1.2 LHC AND ATLAS EXPERIMENT

1.2.1 Large Hadron Collider

The Large Hadron Collider (the LHC) is a particle accelerator of 27 km in circumference, which spans Swiss and French borders. The LHC is the largest and most-energetic particle accelerator built to date, designed to probe the TeV energy scale in proton-proton and Pb-Pb collisions. It is hoped that the LHC will shed light on some of the most important current questions in physics concerning fundamental forces. The LHC data are being already used to study the SM Higgs boson and to search for phenomena of SUSY, Dark Matter and many other Beyond-the-Standard-Model (BSM) predictions. More detail concerning the current and projected studies at the LHC may be found in References [28] and [29]. An overview of the LHC accelerator complex is shown in in Fig. 3.

The LHC accelerator complex is a chain of accelerators which boost the energy of proton beams in stages. The protons start their accelerating phase in the linear accelerator (LINAC). Before being finally accelerated in the LHC, the protons undergo the intermediate acceleration phases in two synchrotrons: the proton synchrotron (PS) and the super proton synchrotron (SPS). The entire accelerating process can be conceptually divided into four steps: proton production, pre-acceleration, acceleration to desired collision energies, and proton storage. The proton production source is the H^+ ions that are produced in a plasma in a device called the Duoplasmatron. Before being transferred into the LINAC for the first step of acceleration, the ions are shaped into a beam by radio frequency quadrupole magnets. They are then transferred into the PS via the proton synchrotron booster, where protons reach the energy of 1.4 GeV. The PS is the last synchrotron that is responsible for providing the protons bunch spacing in the beam pipe. The beam is then passed to the SPS, where it reaches energies of 450 GeV and is then injected into the LHC. The LHC is the final synchrotron that can, in principle, accelerate protons up to 7 TeV. With 1232 dipole and 386 quadrupole magnets, and with a circumference of 27 km, the LHC is the worlds largest and highest energy particle accelerator. One beam of protons is accelerated in one direction and another beam of protons is accelerated in the opposite direction. [28][29]. Since the op-

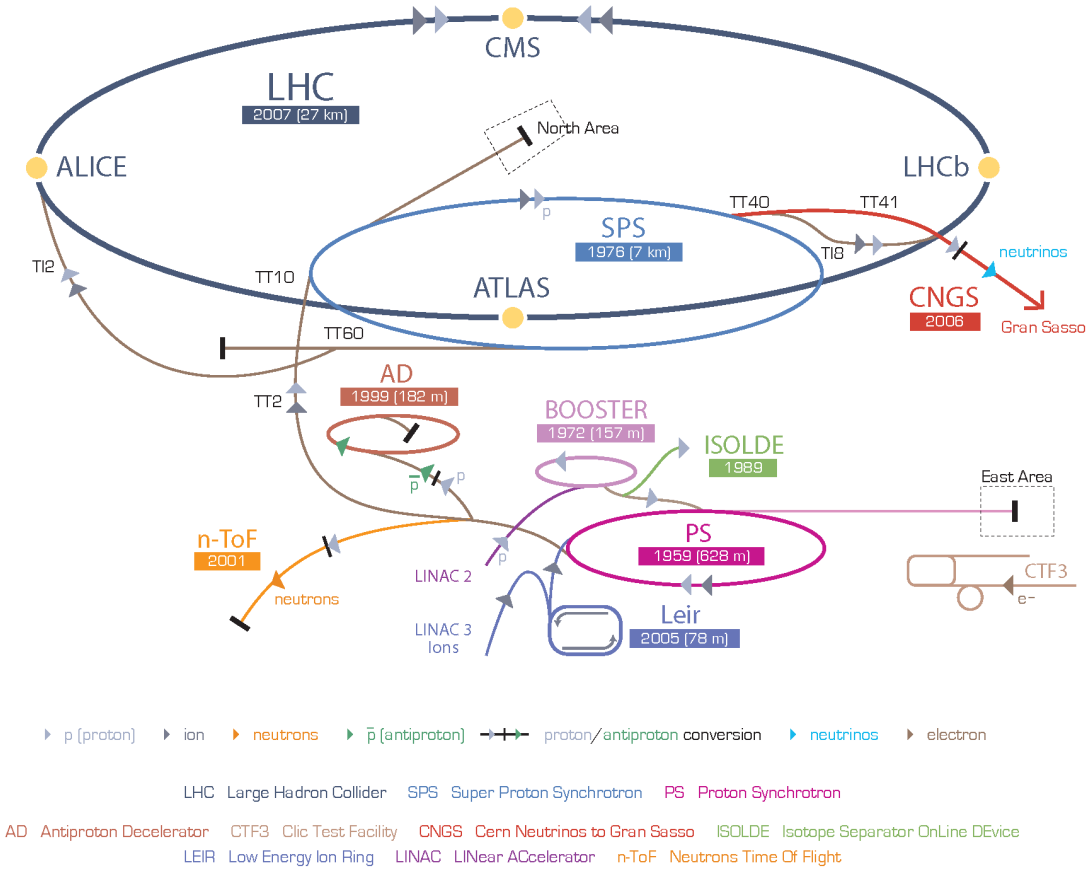

Figure 3: The Large Hadron Collider Accelerator Complex.

erations began in 2009, LHC has delivered 31.23 fb^{-1} of luminosity until its long shutdown phase started in early 2013. During its first stage of operation, the LHC experiments ATLAS and CMS were able to discover the Higgs boson [30] (or the particle whose properties, with limited statistics, are consistent with those expected from the SM Higgs).

1.2.2 ATLAS Detector

ATLAS is a multipurpose experiment and is one of the four main experiments at the LHC. The most important ATLAS properties include a precise electromagnetic calorimetry, which enables efficient identification of electrons and photons in the energy range 5 GeV to 5 TeV with precision better than 0.5%. This is complemented by full-coverage hadronic calorimetry for accurate jet and missing transverse energy (E_{Tmiss}) measurements. The muon spectrometer (MS) provides high-precision muon momentum measurements, with the capability to guarantee accurate measurements at the highest luminosity using the external standalone muon spectrometer. The MS is capable of measuring muons with momenta above 3 GeV, up to 1 TeV. The inner detector provides efficient tracking at high luminosity for high-p_T lepton momentum measurements, electron and photon identification, τ-lepton and heavy-flavour identification. ATLAS detector has a large acceptance in pseudorapidity (η) with almost full azimuthal angle (ϕ) coverage everywhere. The azimuthal angle is measured around the beam axis, whereas pseudorapidity relates to the polar angle (θ) where θ is the angle from the beam axis (in the z direction). Triggering and measurements of particles at low-p_T thresholds, provides high efficiencies for most physics processes of interest at the LHC. The ATLAS trigger system is designed to be able to handle the LHC bunch crossing rate of 40 MHz, and reduce the output events rate down to approximately 200 Hz. The interaction vertex resolution is in the range of $40 - 70$ μm in the z-direction (along the beam pipe). More details may be found in the ATLAS technical design report [31].

The beam direction defines the z-axis, and the $x - y$ plane is transverse to the beam direction. The positive x-axis points from the interaction point to the centre of the LHC ring, and the positive y-axis is pointing upward. The azimuthal angle ϕ is measured around

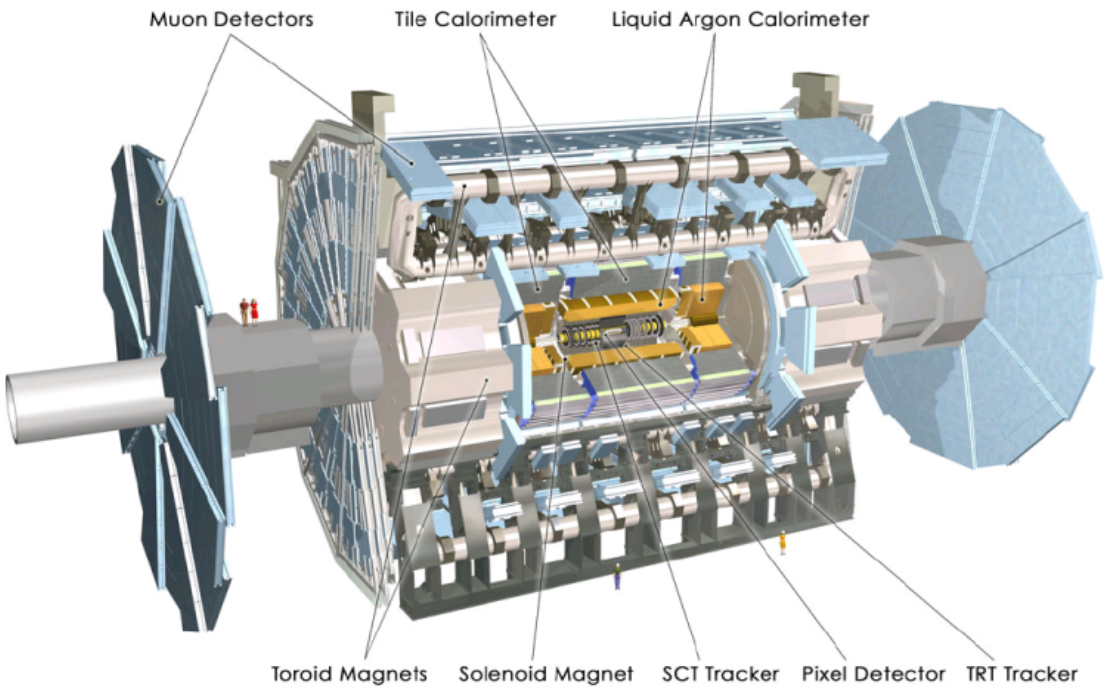

Figure 4: The ATLAS Detector.

the beam axis, and the polar angle θ is measured with respect to the beam axis. The pseudorapidity is defined as $\eta = -ln\,(tan(\theta/2))$. The transverse momentum p_T and the transverse energy[1] E_T, as well as the missing transverse energy E_{Tmiss} and other transverse variables, are defined in the $x-y$ plane unless stated otherwise. The distance ΔR in the pseudorapidity-azimuthal angle space is defined as $\Delta R = \sqrt{(\Delta\eta^2 + \Delta\phi^2)}$.

1.2.2.1 Inner Detector In ATLAS, at the LHC design luminosity of $10^{34}\text{cm}^{-2}\text{s}^{-1}$, approximately 1000 particles emerge from the collision point every 25 ns within $|\eta| < 2.5$, creating a very large track density in the detector. To achieve the momentum and vertex resolution requirements imposed by the benchmark physics processes, high-precision measurements are made in the inner detector (ID), shown in Fig. 5.[32]

The precision tracking detectors (pixels and SCT) cover the region $|\eta| < 2.5$. In the barrel

[1]The ATLAS detector is calibrated so that that the measured energy at a particular colorimetric cell is interpreted as $E\,\sin(\theta)$.

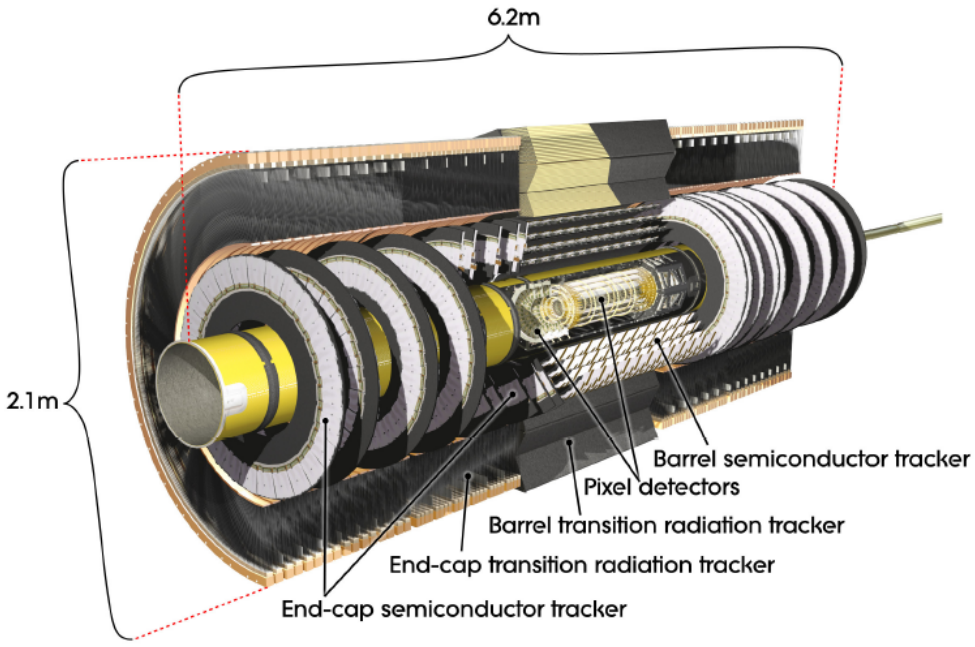

Figure 5: Cut-away view of the ATLAS inner detector.

region, they are arranged on concentric cylinders around the beam axis while in the end-cap regions they are mounted on disks perpendicular to the beam axis. The highest granularity is achieved around the vertex region using silicon pixel sensors. All pixel modules are identical and the minimum pixel size on a sensor is 50 $\times$ 400 μm^2. The pixel layers are segmented in $R-\phi$ and z with typically three pixel layers crossed by each particle. The first layer, called the "vertexing layer", is at a radius of 51 mm. The intrinsic accuracies in the barrel are 10 μm ($R-\phi$) and 115 μm (z) and in the disks are 10 μm ($R-\phi$) and 115 μm (R). The pixel detector has approximately 80.4 million readout channels.

For the SCT, eight strip layers (four space points) are crossed by each track. In the barrel region, this detector uses small-angle (40 mrad) stereo strips to measure both coordinates, with one set of strips in each layer parallel to the beam direction, measuring $R-\phi$. Each side of a detector module consists of two 6.4 cm long, daisy-chained sensors with a strip pitch of 80 μm. In the end-cap region, the detectors have a set of strips running radially and a set of stereo strips at an angle of 40 mrad. The mean pitch of the strips is also approximately

80 μm. The intrinsic accuracies per module in the barrel are 17 μm ($R-\phi$) and 580 μm (z) and in the disks are 17 μm ($R-\phi$) and 580 μm (R). The total number of readout channels in the SCT is approximately 6.3 million.

The TRT contains up to 73 layers of straws interleaved with fibres (barrel) and 160 straw planes interleaved with foils (end-cap), which provide transition radiation for electron identification. All charged tracks with $p_T > 0.5$ GeV and $\eta < 2.0$ will traverse at least 36 straws, except in the barrel-end-cap transition region ($0.8 < |\eta| < 1.0$), where this number decreases to a minimum of 22 crossed straws. Typically, seven to ten high-threshold hits from transition radiation are expected for electrons with energies above 2 GeV. Therefore, a large number of hits are provided by the 4 mm diameter straw tubes of the TRT, which enables track-following up to $|\eta| = 2.0$. The TRT only provides $R-\phi$ information, for which it has an intrinsic accuracy of 130 μm per straw. In the barrel region, the straws are parallel to the beam axis and are 144 cm long, with their wires divided into two halves, approximately at $\eta = 0$. In the end-cap region, the 37 cm long straws are arranged radially in wheels. The total number of TRT readout channels is approximately 351,000 [31].

1.2.2.2 Electromagnetic Calorimeter The precision electromagnetic calorimeters are lead-liquid argon sampling detectors with accordion-shaped absorbers and electrodes. This geometry allows the calorimeters to have several active layers in depth: three in the precision-measurement region ($0 < |\eta| < 2.5$) which is the Barrel part of the detector (see Fig. 8) and two in the higher-η region ($2.5 < |\eta| < 3.2$) which are known as the Endcaps of the EM calorimeter (EMEC). The overlap region between the barrel and the EMEC also has two active layers. In the precision measurement region, an accurate position measurement is obtained by finely segmenting the first layer in η. The η-direction of photons is determined by the position of the photon cluster in the first and the second layers. The calorimeter system also has electromagnetic coverage at higher η ($3.1 < |\eta| < 4.9$) provided by the FCal (Forward Calorimeter. See Fig. 8). Furthermore in the region ($0 < |\eta| < 1.8$) the electromagnetic calorimeters are complemented by presamplers, an instrumented argon layer, which provides a measurement of the energy lost in front of the electromagnetic calorimeters. More details could be found in Ref. [33].

An accordion geometry has been chosen for the absorbers and the electrodes of the barrel and endcap electromagnetic calorimeters (see Fig. 6 and Fig. 7). Such a geometry provides naturally a full coverage in ϕ without any cracks, and a fast extraction of the signal at the rear or at the front of the electrodes. In the barrel, the accordion waves are axial and run in ϕ, and the folding angles of the waves vary with radius to keep the liquid-argon gap constant. In the end-caps, the waves are parallel to the radial direction and run axially. Since the liquid-argon gap increases with radius in the end-caps, the wave amplitude and the folding angle of the absorbers and electrodes vary with radius (see Fig. 7). All these features of the accordion geometry lead to a very uniform performance in terms of linearity and resolution as a function of ϕ.

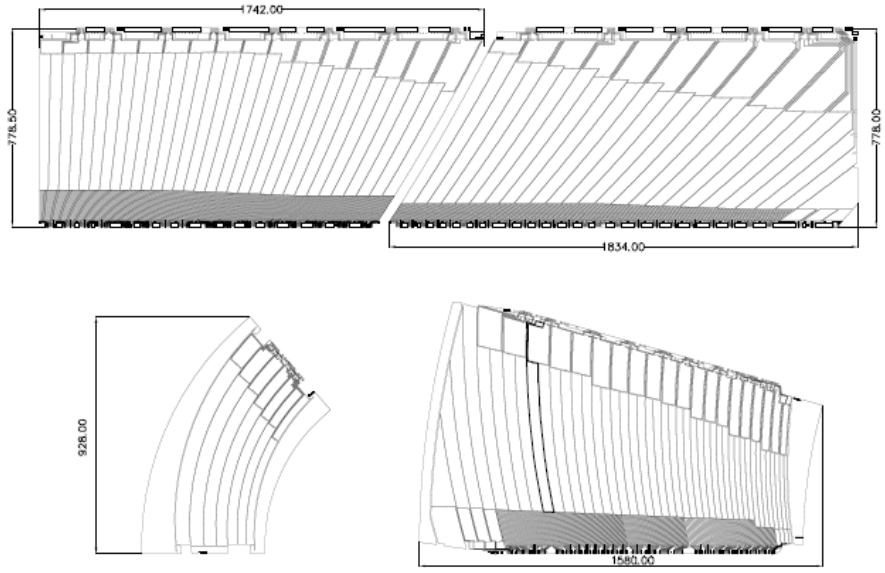

Figure 6: Layout of the signal layer for the four different types of electrodes before folding. The two top electrodes are for the barrel and the two bottom electrodes are for the end-cap inner (left) and outer (right) wheels. Dimensions are in millimetres. The drawings are all at the same scale. The two or three different layers in depth are clearly visible.

The absorbers are made of lead plates, to which two stainless-steel sheets (0.2 mm thick) are glued using a resin-impregnated glass-fibre fabric to provide mechanical strength. The lead plates in the barrel have a thickness of 1.53 mm for $|\eta| < 0.8$ and of 1.13 mm for $\eta > 0.8$. The change in lead thickness at $|\eta| = 0.8$ limits the decrease of the sampling fraction as $|\eta|$

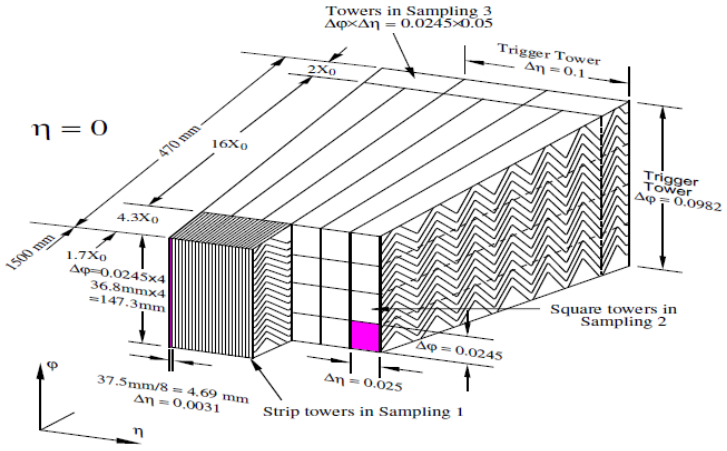

Figure 7: Sketch of a barrel module where the different layers are clearly visible with the ganging of electrodes in ϕ. The granularity in η and ϕ of the cells of each of the three layers and of the trigger towers is also shown.

increases. In the end-cap calorimeters, the plates have a thickness of 1.7 mm for $|\eta| < 2.5$ and of 2.2 mm for $|\eta| > 2.5$.

The readout electrodes are located in the gaps between the absorbers and consist of three conductive copper layers separated by insulating polyimide sheets. The two outer layers are at the high-voltage potential and the inner one is used for reading out the signal via capacitive coupling. The segmentation of the calorimeter in η and in depth is obtained by etched patterns on the different layers, as shown in Fig. 6.

1.2.2.3 Hadronic Calorimeter The hadronic calorimeters of ATLAS is constructed from three main subsystems. In the barrel region ($|\eta| < 1.7$) there is the scintillating tile calorimeter. The Hadronic End-cap LAr Calorimeter (HEC) extends up to $|\eta| = 3.2$. The range $3.1 < |\eta| < 4.9$ is covered by the high density Forward Calorimeter (FCAL) [32] [34].

The tile calorimeter is a sampling calorimeter that uses steel as the absorber and scintillator as the active medium. It is located in the region $|\eta| < 1.7$, behind the liquid argon electromagnetic calorimeter and is subdivided into a central barrel, 5.8 m in length, and two

extended barrels, 2.6 m in length and each having an inner radius of 2.28 m and an outer radius of 4.25 m, as shown in Fig. 8. The radial depth of the tile calorimeter is approximately 7.4λ (hadronic interaction lengths). Each barrel consists of 64 modules or wedges of size $\Delta\phi \approx 0.1$, made of steel plates and scintillating tiles [34].

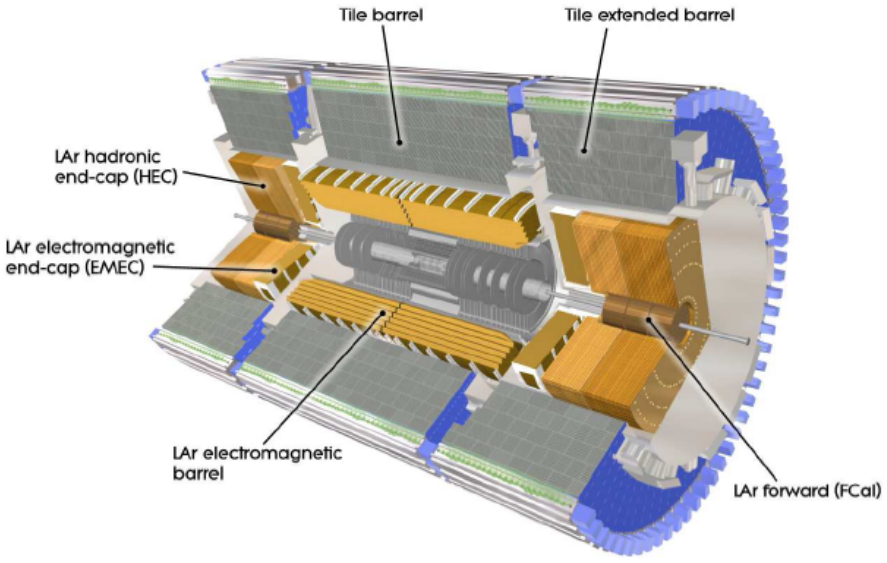

Figure 8: Cut-away view of the ATLAS calorimeter system.

The assembled module forms an almost-periodic steel-scintillator structure with a ratio by volume of approximately 4.7:1. The orientation of the scintillator tiles radially and normal to the beam line, in combination with wavelength-shifting fibre readout on the tile edges, allows for almost seamless azimuthal calorimeter coverage. The grouping of the readout fibres into the readout photomultiplier tubes (PMTs) provides an approximately projective geometry in pseudorapidity. The gap region between the barrel and the extended barrel is instrumented with special modules, made of steel-scintillator sandwiches with the same sampling fraction as the rest of the tile calorimeter and with thin scintillator counters in the sectors where the available space in the gaps is even more limited. These devices allow us to partially recover the energy lost in the crack regions of the detector.

The electronics and readout of the tile calorimeter are highly integrated with the mechanical structure. The photomultiplier tubes and all the front-end electronics are mounted in 1.4 m long aluminium units, called drawers, which are inserted inside the support girder

at the rear of each module. The front-end electronics also provide analogue sums of subsets of the channels, forming trigger towers, for the Level one (L1) trigger (see section 1.2.2.5 for explanation). The low-voltage power supplies which power the readout are mounted in an external steel box, which has the cross-section of the support girder and which also contains the external connections for power and other services for the electronics. Finally, the calorimeter is equipped with three calibration systems: charge injection, laser and a ^{137}Cs radioactive source.

The hadronic end-cap calorimeter (HEC) [34] is a copper/liquid-argon sampling calorimeter with a flat-plate design, which covers the range $1.5 < |\eta| < 3.2$. The HEC consists of two wheels in each end-cap cryostat: a front wheel (HEC1) and a rear wheel (HEC2), each wheel containing two longitudinal sections. The wheels are cylindrical with an outer radius of 2030 mm. Each of the four HEC wheels is constructed of 32 identical wedge-shaped modules. A stainless-steel connecting-bar system at the outer wheel perimeter guarantees the mechanical integrity of the wheel structure. At the inner radius, small copper connecting bars link the plates of each set of neighbouring modules. Two sliding rails support the wheels inside the cryostat and are an integral part of the mechanical structure. The final vertical deformation of the wheel structure has been measured for the four wheels to represent a sag of 0.3 mm on average. The wheels remain perpendicular to their axis within ± 1.0 mm.
The modules of the front wheels are made of 24 copper plates, each 25 mm thick, plus a 12.5 mm thick front plate. In the rear wheels, the sampling fraction is coarser with modules made of 16 copper plates, each 50 mm thick, plus a 25 mm thick front plate. The gaps in between the plates all have a thickness of 8.5 mm. The resulting sampling fractions for HEC1 and for HEC2 are 4.4% and 2.2% respectively. The wheels have an inner radius of 372 mm for the first nine plates of HEC1 and of 475 mm for the remaining plates of HEC1 and for all 17 plates of HEC2. The structural strength of the modules is provided by seven stainless-steel tie-rods with 12 mm (16 mm) diameter for the front (rear) modules. Annular high-precision spacers on the tie-rods maintain the 8.5 mm gaps between the copper plates.

The forward calorimeters (FCal) are located in the same cryostats as the end-cap calorimeters and provide coverage over $3.1 < |\eta| < 4.9$. The close vicinity and coupling between these systems result in a quite hermetic design, which minimises energy losses in

cracks between the calorimeter systems and also limits the backgrounds which reach the muon system. As the FCal modules are located at high η, at a distance of approximately 4.7 m from the interaction point, they are exposed to high particle fluxes. This has resulted in a design with very small liquid-argon gaps, which have been obtained by using an electrode structure of small-diameter rods, centred in tubes which are oriented parallel to the beam direction. The liquid-argon gaps are smaller than the usual 2mm gap of the electromagnetic barrel calorimeter to avoid ion build-up problems and to provide at the same time the highest possible density. These smaller gaps also lead to a faster signal with roughly the same instantaneous current but smaller integrated current. In the electromagnetic layer (FCal1), the triangular current pulse at the electrode has a full drift time of 60 ns. For FCal2 and FCal3, the full drift time scales with the gap size since the field in the gaps is similar for all three modules.

1.2.2.4 Muon Spectrometer The muon spectrometer forms the outer part of the ATLAS detector and is designed to detect charged particles exiting the barrel and end-cap calorimeters and to measure their momentum in the pseudorapidity range $|\eta| < 2.7$. It is also designed to trigger on muons in the region $|\eta| < 2.4$. The driving performance goal is a stand-alone transverse momentum resolution of approximately 10% for 1 TeV tracks. Muon momenta down to a few GeV ($\sim$ 3 GeV, due to energy loss in the calorimeters) may be measured by the spectrometer alone. Even at the high end of the accessible range ($\sim$ 3 TeV), the stand-alone measurements still provide adequate momentum resolution and excellent charge identification [35].

Precision-tracking chambers in the barrel region are located between and on the eight coils of the superconducting barrel toroid magnet, while the end-cap chambers are in front and behind the two end-cap toroid magnets. The ϕ symmetry of the toroids is reflected in the symmetric structure of the muon chamber system, consisting of eight octants. Each octant is subdivided in the azimuthal direction in two sectors with slightly different lateral extensions, a large and a small sector, leading to a region of overlap in ϕ. This overlap of the chamber boundaries minimises gaps in detector coverage and also allows for the relative alignment of adjacent sectors using tracks recorded by both a large and a small chamber.

The chambers in the barrel are arranged in three concentric cylindrical shells around the beam axis at radii of approximately 5 m, 7.5 m, and 10 m. In the two end-cap regions, muon chambers form large wheels, perpendicular to the z-axis and located at distances of $|z| \approx 7.4$ m, 10.8 m, 14 m, and 21.5 m from the interaction point. Figures 9 and 10 give cross-sections in the planes transverse to, and containing, the beam axis. In the centre of the detector, a gap in chamber coverage has been left open to allow for services to the solenoid magnet, the calorimeters and the inner detector. The size of the gap varies from sector to sector depending on the service necessities, the biggest gaps of 1-2 m being located in the large sectors. The precision momentum measurement is performed by the Monitored

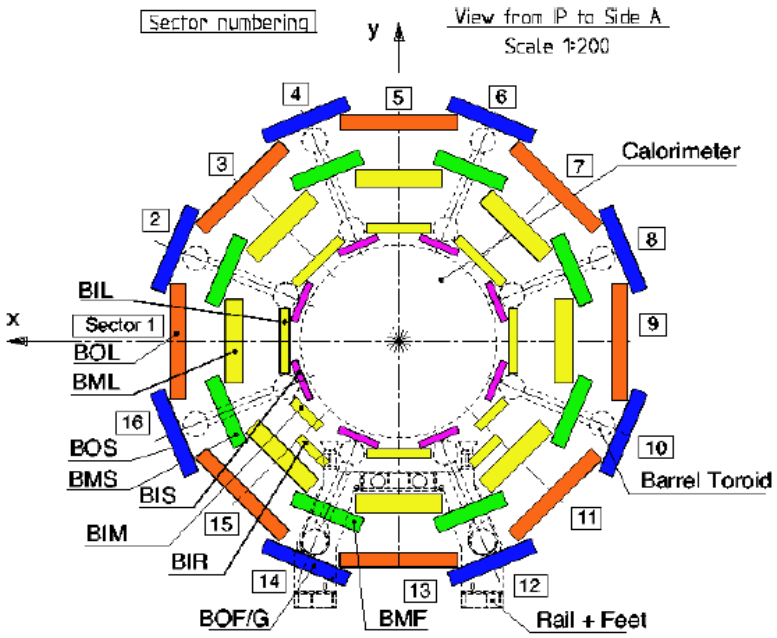

Figure 9: Cross-section of the barrel muon system perpendicular to the beam axis (non-bending plane), showing three concentric cylindrical layers of eight large and eight small chambers. The outer diameter is about 20 m.

Drift Tube chambers (MDTs), which combine high measurement accuracy, predictability of mechanical deformations and simplicity of construction. They cover the pseudorapidity range $|\eta| < 2.7$ (except in the innermost end-cap layer where their coverage is limited to $|\eta| < 2.0$). These chambers consist of three to eight layers of drift tubes, operated at an

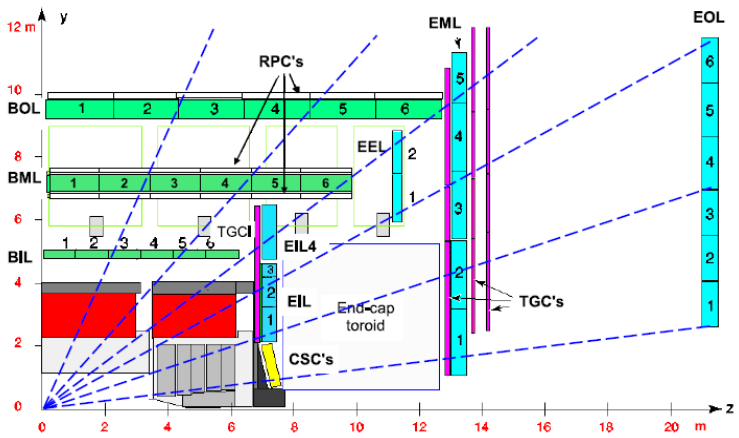

Figure 10: Cross-section of the muon system in a plane containing the beam axis (bending plane). Infinite-momentum muons would propagate along straight trajectories which are illustrated by the dashed lines and typically traverse three muon stations.

absolute pressure of 3 bar, which achieve an average resolution of 80 mm per tube, or about 35 mm per chamber.

In the forward region ($2.0 < |\eta| < 2.7$), Cathode-Strip Chambers (CSC) are used in the innermost tracking layer due to their higher rate capability and time resolution. The CSCs are multiwire proportional chambers with cathode planes segmented into strips in orthogonal directions. This allows both coordinates to be measured from the induced-charge distribution. The resolution of a chamber is 40 mm in the bending plane and about 5 mm in the transverse plane. The difference in resolution between the bending and non-bending planes is due to the different readout pitch, and to the fact that the azimuthal readout runs parallel to the anode wires.

1.2.2.5 Trigger System The ATLAS trigger [32] is composed of three levels of event selection: Level 1 (L1) which is hardware-based, the Level 2 and Event Filter (EF) (collectively referred to as the High Level Trigger or HLT) based on software algorithms analyzing the data on large computing farms. The three levels of the ATLAS trigger system must reduce the output event storage rate to $\sim$ 200 Hz from an initial LHC bunch crossing rate

of 40 MHz. The ATLAS trigger system is schematically shown in Fig. 11. It is evident from Fig. 12 that large rejection against QCD processes is needed while maintaining high efficiency for low cross section physics processes that include processes for new physics.

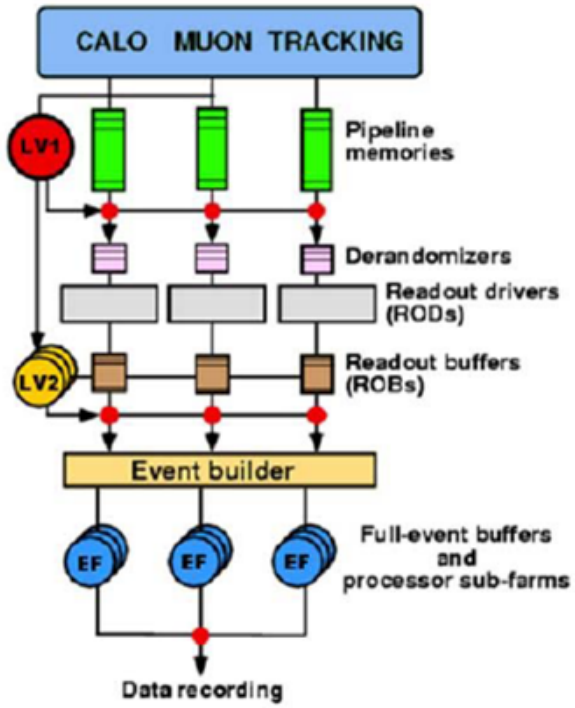

Figure 11: A schematic representation of the ATLAS trigger system.

The L1 trigger system receives data at the full LHC bunch crossing rate of 40 MHz and must make its decision within 2.5 μs to reduce the output rate to 75 kHz. The L1 trigger has dedicated access to data from the calorimeter and muon detectors. The L1 calorimeter trigger decision is based on the multiplicities and energy thresholds of the following objects observed in the ATLAS Liquid Argon and Tile calorimeter sub-system: Electromagnetic (EM) clusters, taus, jets, missing transverse energy (E_{Tmiss}), scalar sum transverse energy ($\sum E_T$) in calorimeter, and total transverse energy of observed L1 jets ($\sum E_T$(jets)). These objects are computed by the L1 algorithms using the measured E_T values in trigger towers of 0.1×0.1 granularity in $\Delta\eta \times \Delta\phi$. The L1 muon trigger uses measurement of trajectories in the different stations of the muon trigger detectors: the Resistive Plate Chambers (RPC) in the barrel region and the Thin Gap Chambers (TGC) in the endcap region. The input to

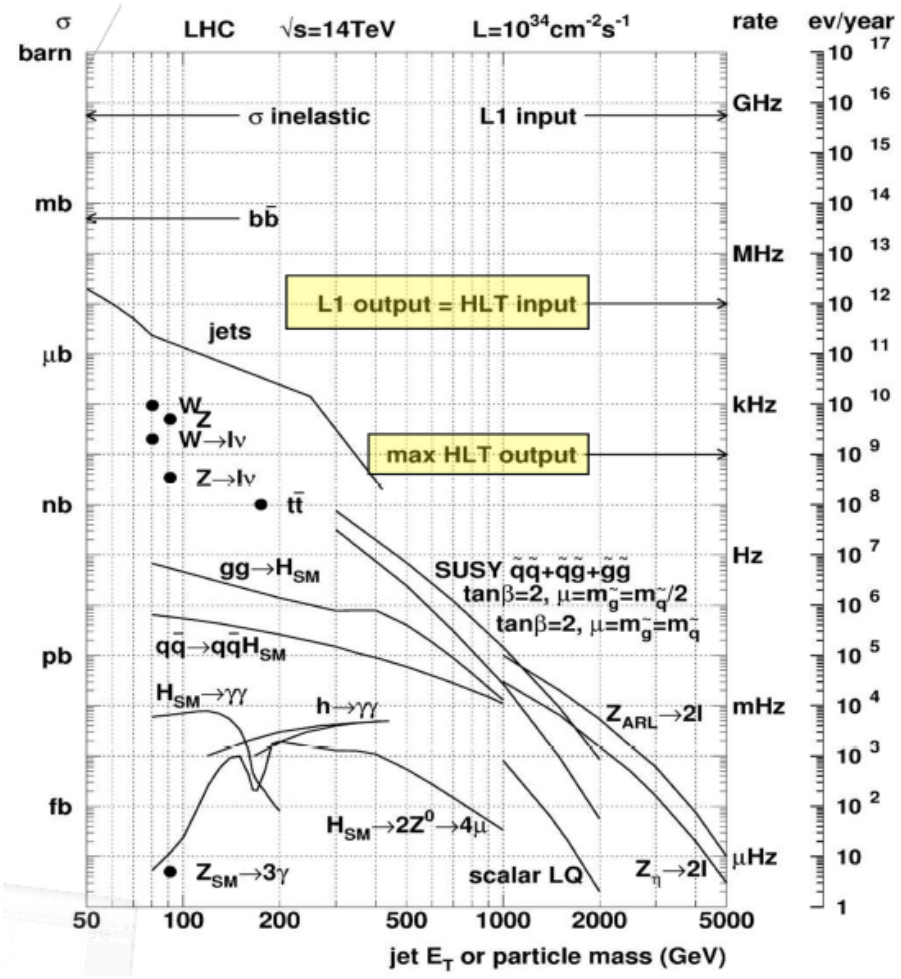

Figure 12: Estimated event rates for several physics processes at the LHC design luminosity.

the trigger decision is the multiplicity for various muon p_T thresholds.

The L2 trigger is software-based, with the selection algorithms running on a farm of commodity PCs. The selection is largely based on regions-of-interest (RoI) identified at L1 and uses fine-grained data from the detector for a local analysis of the L1 candidate. A seed is constructed for each trigger accepted by L1 that consists of a p_T threshold and an $\eta - \phi$ position. The L2 algorithms use this seed to construct an RoI window around the seed position. The size of the RoI window is determined by the L2 algorithms depending on the type of triggered object (for example, a smaller RoI is used for electron triggers than for jet triggers). The L2 algorithms then use the RoI to selectively access, unpack and analyze the associated detector data for that $\eta-\phi$ position. The ability to move, unpack, and analyse the local data only around the seed position greatly reduces both the processing times and the required data bandwidth. The L2 algorithms provide a refined analysis of the L1 features based on fine-grained detector data and more optimal calibrations to provide results with improved resolution. They provide the ability to use detector information that is not available at L1, most notably reconstructed tracks from the Inner Detector. The information from individual sub-systems can then be matched to provide additional rejection and higher purity at L2. For each L1 RoI, a sequence of L2 algorithms is executed which compute event feature quantities associated with the RoI. Subsequently, a coherent set of selection criteria is applied on the derived features to determine if the candidate object should be retained.

The final online selection is performed by software algorithms running on the Event Filter (EF), a farm of processors that consist of 1800 dual quad-core CPUs. The EF receives events accepted by L2 at a rate of 2 kHz (1 kHz) during nominal (startup) operations and must provide the additional rejection to reduce the output rate to $\sim$ 200 Hz. An average processing time of 4 s per event is available to achieve this rejection. The output rate from the Event Filter is limited by the offline computing budget and storage capacity. As in L2, the EF works in a seeded mode, although it has direct access to the complete data for a given event as the EF selection is performed after the event building step. Each L2 trigger that has been accepted can be used to seed a sequence of EF algorithms that provide a more refined and complete analysis. Unlike L2, which uses specialized algorithms optimized for timing performance, the EF typically uses the same algorithms as the offline reconstruction.

The use of the more complex pattern recognition algorithms and calibration developed for offline helps in providing the additional rejection needed at the EF.

2.0 DATA, SIGNAL AND BACKGROUNDS

In this chapter we describe the data used in the analysis, estimation of signal and background using MC samples and data driven QCD background estimation. Also the object selection and event selection are described.

2.1 DATA SAMPLES

By the time the LHC stopped for a long planned shutdown in February of 2013, ATLAS has recorded data sample equivalent to 27.03 fb^{-1}, bulk of which was collected during 2012. This thesis, however, is based on data corresponding to 4.7 fb^{-1} of the integrated pp luminosity collected by the end of 2011. This is because, at the time when this thesis was written, a large fraction of the most recently recorded data has not yet been properly calibrated and validated, so was not yet released for the analysis. Data collection periods are summarized in Table 1, along with the trigger configurations that were used during each individual period.

2.2 MONTE CARLO SAMPLES

All signal and background samples are generated using the ATLAS underlying event tunes [37] and processed through the ATLAS detector simulation [38] based on GEANT4 [39]. The MC samples are produced including the simulation of multiple interactions per LHC bunch crossing (pile-up). Varying pile-up conditions and their dependence on the instantaneous

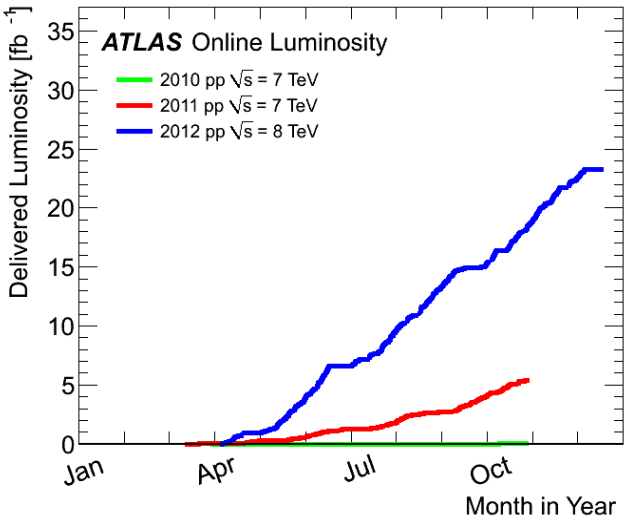

Figure 13: Recorded cumulative luminosity collected with ATLAS versus time [40].

luminosity of the LHC are taken into account by reweighting MC events to match the pile-up conditions measured in data.

As a member of ATLAS responsible for various aspects of MC simulation, the author of this thesis made contributions to maintaining ATLAS interface to PHOTOS package, which simulates radiative corrections in decays.

2.2.1 Left Right Symmetric Model Signal MC

Signal Monte Carlo samples we generated for ATLAS were prepared using PYTHIA [36]. LRSM model implemented in PYTHIA is according to "Doubly Charged Higgs at LHC" [11]. The implementation in PYTHIA is by A.Ferrari and J.Collot whose previous ATLAS studies based on ATLFAST are described in [12] and in ATLAS preprints [43] and [44].

PYTHIA 6 [36] MC generator was used to simulate LRSM signal MC samples. Simulation was performed using ATLAS offline software release 16.6.4.2, later reprocessed with release 17. The considered W_R mass range is between 600 GeV and 2700 GeV, which is a sufficient range for setting limits for the collected integrated luminosity. The mass of heavy neutrino

Period	Trigger	Recorded Luminosity (pb^{-1})
B	EF_MU18_MG	11.738
D	EF_MU18_MG	166.649
E	EF_MU18_MG	48.657
F	EF_MU18_MG	136.097
G	EF_MU18_MG	537.482
H	EF_MU18_MG	259.46
I	EF_MU18_MG	337.542
J	EF_MU18_MG_MEDIUM	226.392
K	EF_MU18_MG_MEDIUM	590.364
L	EF_MU18_MG_MEDIUM	1401.869
M	EF_MU18_MG_MEDIUM	1025.622
		4741.872

Table 1: Data Collection Periods and respective trigger configurations. The trigger mnemonics are explained in the text (section 2.4).

is assumed to be less than that of W_R. Several heavy neutrino mass points are studied for each value of the W_R mass. For each mass point approximately 20,000 signal MC events were generated.

Figure 14 shows kinematic distributions for a representative signal sample of $M(W_R) =$ 800 GeV, $M(N) = 300$ GeV. The distributions for η shows that the more than 80% of the signal muons are inside $|\eta| < 2.5$, the middle part of the detector where the detection efficiency high.

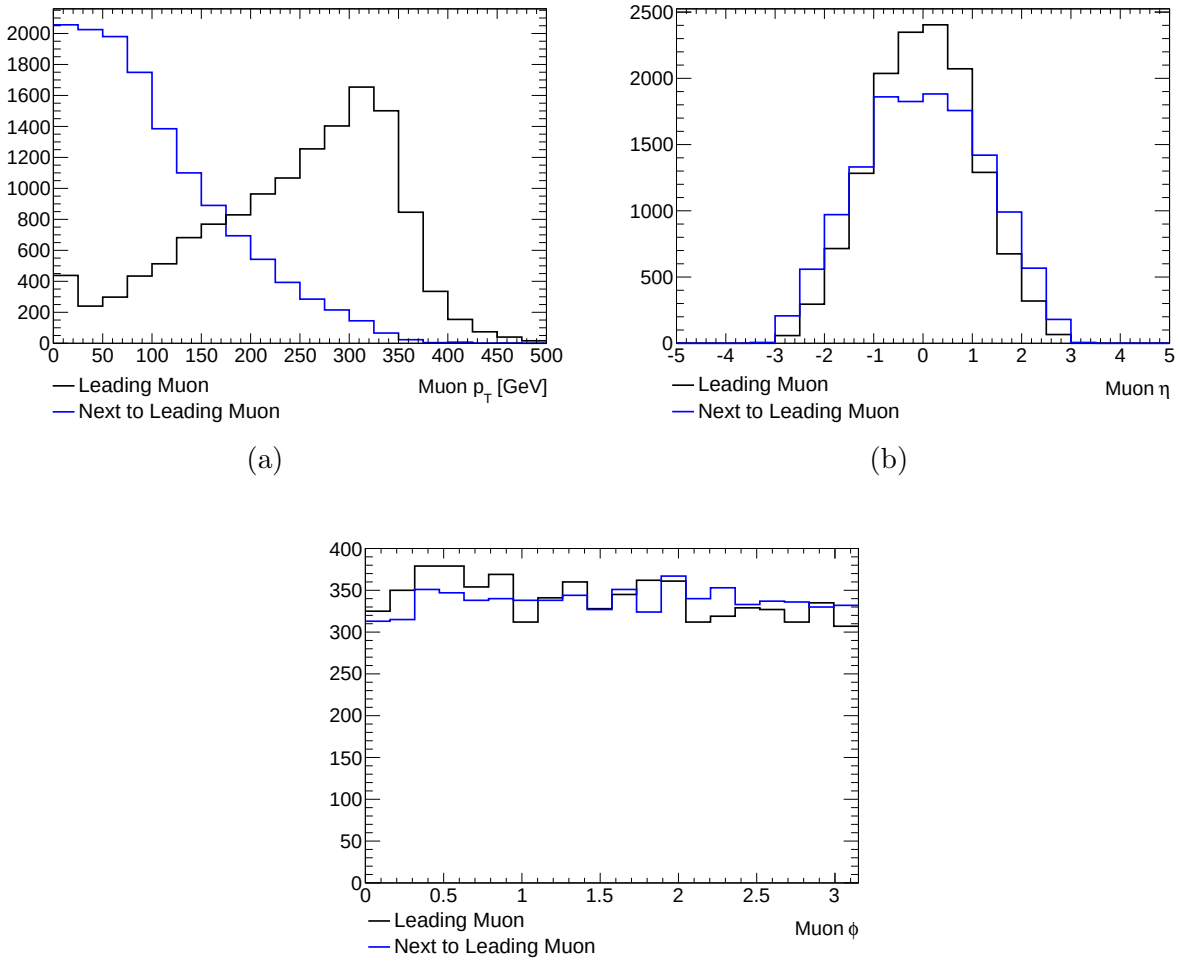

(a) (b)

(c)

Figure 14: p_T (top-left), η (top-right) and ϕ (bottom) distributions of two signal muons in a representative signal sample $M(W_R) = 800$ GeV, $M(N) = 300$ GeV.

2.2.2 Standard Model Backgrounds

The signal events consists of two muons and at least 1 jet. Several categories of SM background which mimicks the signal signature were studied using MC samples. QCD background was studied using fake matrix method described in Section 2.5. The SM backgrounds important for our analysis include

- Z+jets and W+jets generated using MadGraph [52] with a filter requiring at least one lepton.
- $t\bar{t}$ and single-top samples were generated using MC@NLO [53, 54]. The top quark mass was set to 172.5 GeV. A filter was applied to select events with at least one lepton.
- Dibosons (WW, WZ and ZZ samples) were generated with HERWIG [55] with a filter requiring at least one lepton. Associated production of W and Z bosons with a $t\bar{t}$ pair has been studied with $t\bar{t}$+W, $t\bar{t}$+W+jet, $t\bar{t}$+WW and $t\bar{t}$+Z MC samples which were generated with MadGraph interfaced to PYTHIA for hadronization.

2.3 OBJECT PRESELECTION

To ensure high quality object reconstruction for signal event candidates, to improve the invariant mass resolution and to reduce systematic uncertainties, the reconstructed objects such as muon and electron candidates and jets are required to satisfy additional selection criteria described in this section.

2.3.1 Muons

We use muon candidates reconstructed with STACO (STAtistical COmbination) package, which is one of the two muon reconstruction algorithms [46] used on ATLAS. According to our studies STACO is deemed to be more suitable for the discussed search with high-momentum muons. Muon candidates are reconstructed independently in the inner detector and in the muon spectrometer. In our analysis we select STACO candidates that have tracks reconstructed in both subsystems. Muon with the leading transverse momentum is required

to have $p_T > 25$ GeV, and sub-leading muon is required to have $p_T > 20$ GeV. The cutoff on p_T suppresses background from SM events. Muons are required to be have $|\eta| < 2.5$, where muons can trigger the event. Curvature of the muon's tracks in the inner detector and muon spectrometer is required to be same, to greately suppress charge mis-identification (probability of analysis muons to have charge mis-identification is less than 1 in a 100,000). Muons are required to have their tracks to be in close vicinity of the primary interaction point to reject muons from cosmic rays.

Such requirements are placed to maximize the signal efficiency while effectively suppressing the backgrounds arising from SM processes. Both muons candidates are required to have $|\eta| < 2.5$. This is the region of the detector where a charged particle traverses all tracking susbsystems and, also, single-particle trigger efficiency reaches 98%. The following additional criteria are imposed for each STACO candidate:

- A b-layer hit is required (if expected)
- The number of hits in the pixel layer added to the number of crossed dead pixel sensors must be greater than 1
- The number of SCT hits added to the number of crossed dead SCT sensors must be $>= 6$
- The number of pixel holes added to the number of SCT holes should be < 3
- For $|\eta| < 1.9$, require $N_{hits} + N_{outliers} > 5$ and $N_{outliers} < 0.9 \cdot (N_{hits} + N_{outliers})$
- For $|\eta| \geq 1.9$, if $N_{hits} + N_{outliers} > 5$, we require $N_{outliers} < 0.9 \cdot (N_{hits} + N_{outliers})$

To select high-quality muon candidates and to reduce background from QCD events, the curvatures of the muon's track reconstructed in the inner detector and in the muon spectrometer are required to be of the same sign. Several criteria on the track impact parameters are imposed such that, two muon candidates are required to originate from the same primary vertex, an important requirement for events with multiple interactions because this criterion is powerful at reducing non prompt muons from QCD processes.

Furthermore, muon candidates in the event are required to be *isolated*, where the isolation criteria are defined below. The parameter $E_{Tcone20}$ is defined as energy deposited in the calorimeter inside a cone radius of $\Delta R < 0.2$ around the direction of the muon track.

- When a muon candidate is close to a jet within $\Delta R < 0.4$ we require
  - muon $p_T > 80$ GeV
  - $(E_{Tcone20} - 1\text{GeV})/p_T < 0.05$ OR $Mass(\mu, jet_{closest})Mass(jet_{closest}) < 10GeV$
- If muon is not close to a jet
  - $(E_{Tcone20} - 1\text{GeV})/p_T < 0.05$
  - If muon $P_T < 80$ GeV; require $p_{tcone30}/p_T < 0.05$

2.3.2 Electrons

The ATLAS standard cluster-based algorithm is employed for reconstructing electron candidates [32]. The pseudorapidity of the electron cluster is required to be $|\eta| < 2.47$, excluding the EM barrel-endcap overlap region $1.37 < |\eta| < 1.52$. The transverse energy of the electron candidate is required to be $E_T > 20$ GeV. To ensure higher object reconstruction quality and to suppress QCD and $t\bar{t}$ backgrounds the ID track associated with the electron candidate is required not to overlap with an inner detector track of any muon candidate. Furthermore, to suppress poorly reconstructed electrons and to reduce non-prompt electrons from QCD background the impact parameters of the electron's ID track are required to be close to a primary vertex of interaction: $|d_0| < 0.2$ mm, $|z_0| < 0.5$ mm and $|d_{0significance}| < 5$.

2.3.3 Jets

Jets are reconstructed using *AntiKt4TopoEMJets* algorithm, which is an iterative seeded fixed-cone jet finder. When a cluster of calorimeter cells registers energy deposits, that cluster is used as a seed to combine all objects within a cone in pseudorapidity η and azimuth ϕ with $\Delta\ R = \sqrt{\Delta\eta^2 + \Delta\phi^2} < R_{\text{cone}}$, where R_{cone} is the fixed cone radius. A new direction is calculated from the four-momenta inside the initial cone and a new cone is centered around it. Objects are then (re-)collected in this new cone, and again the direction is updated. This process continues until the direction of the cone does not change anymore after recombination, at which point the cone is considered stable and is called a jet. [45, 32].

To be selected, jets are required to have transverse momenta $P_T > 20$ GeV. Jet clusters are required to have pseudorapidity $|\eta| < 2.8$. Furthermore jets from pileup vertices are

rejected. To remove the duplication with electrons, each jet closest to each already selected electron candidate is removed when the seperation between the jet and the electron is less than 0.5 in ΔR .

2.4 EVENT SELECTION

To be selected for further analysis an event is required to have exactly two muon candidates, and no electron candidates (after all selection criteria are applied to select muon and electron candidates). These two muons are required to have their tracks associated with the same primary vertex. Also, at least one jet is required to be present in the event. This last requirement allows for events where signal jets from the decay of heavy neutrino N merged into one hadronic cluster in the calorimeter.

Also, at least one of the two muon candidates must have triggered the event, with trigger threshold $P_T > 20$ GeV. Two trigger configurations were used during the course of data collection in 2011. From data taking periods B-I, the trigger configuration EF_MU18_MG was used, while for data periods J-M, EF_MU18_MG_MEDIUM was used. The prefix EF (Event Filter) denoted the last phase of trigger level 1.2.2.5. MU18 signifies that the trigger seed passed the criteria of having at least $18 - GeV$ energy. MG stands for MuGirl trigger reconstruction algorithm. The postfix MEDIUM in the latter trigger configuration implies further isolation criteria were applied.

Events where detector behavior was problematic were rejected using the following requirements.

Treatment of *bad* jets Reject events where any number of bad LOOSE jets with $p_T > 20$ GeV was found. Such "jets" were found to be detector artifacts associated with malfunctioning front-end electronics.

LAr noise bursts Due to random but non frequent detector electronics misbehavior, the liquid argon calorimeter is seen to report high level energy deposits. Events where such noise bursts were present in the EM calorimeter were rejected.

Objects in the LAr hole Events where an electron or a jet was reconstructed in a problematic region of the EM calorimeter (known as the "LAr hole") were rejected. This problem was present only in data periods E through H.

When the MC simulation is used to estimate the detection efficiency, the detector-induced effects are properly taken into account in the MC simulation.

2.4.1 Additional Criteria for Background Suppression

Further background suppression is achieved by applying a cutoff criteria on dimuon mass, mass of W_R candidate and sum of E_T of final state objects. The suitable cutoff values were chosen such that, signal is not compromised while the background is suppressed as much as possible. According to Fig. 15 the additional background suppression criteria are chosen to be:

- $M(\mu\mu) > 110$ GeV to reduce contribution from Z+jets contribution,
- $M(\mu\mu j(j)) > 400$ GeV,
- Sum of E_T, $S_T > 400$ GeV. This selection criteria is applied only to the events with opposite sign muon pairs since low statistics in same sign events.

2.5 QCD BACKGROUND AND FAKE MATRIX METHOD

The fake matrix method is used to estimate background contributions which include non-prompt leptons. Such processes include semileptonic decays of b and c quarks inside a jet and decays of $\pi^{\pm}$ and K mesons in flight. Non-prompt leptons originating from QCD processes are also known as *fake* leptons (as the flavor of final state lepton is different from the flavor of the quark whose decay it is associated with), from which the name of the method is derived. Few definitions necessary to explain the fake matrix method follow:

Fake lepton Leptons from QCD processes

Real lepton Leptons from non-QCD processes

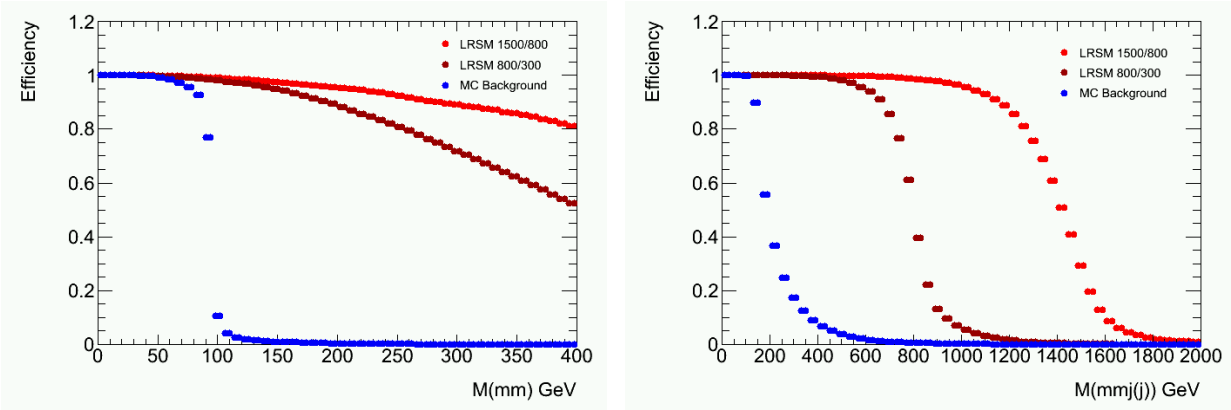

(a) (b)

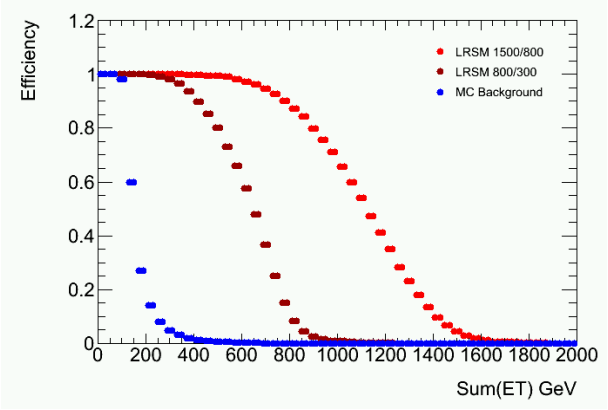

(c)

Figure 15: Efficiencies of two LRSM signals and background estimates from MC are compared. (Top)Efficiency vs. the value of selection criterion applied to the invariant mass of dimuon. (Middle) Efficiency vs. the value of selection criterion applied to the invariant mass of $\mu\mu$-jet(s) combination. (Bottom) Efficiency vs. the value of selection criterion applied to E_T of the $\mu\mu$-jet(s) combination.

Loose Lepton A lepton is defined to be loose if it does not satisfy the isolation requirement (for muons this is explained in Section 2.3.1)

Tight lepton A lepton is defined to be tight if it satisfies the isolation requirement

Real Efficiency Real efficiency r is the probability for a real lepton to have passed the isolation criteria (*i.e*, such lepton is reconstructed as *tight*)

Fake Rate Fake rate f is the probability for a fake lepton to have passed the isolation criteria.

Note that "fake" and "real" classify leptons according to their origin, while "loose" and "tight" describe the quality of reconstructed candidates.

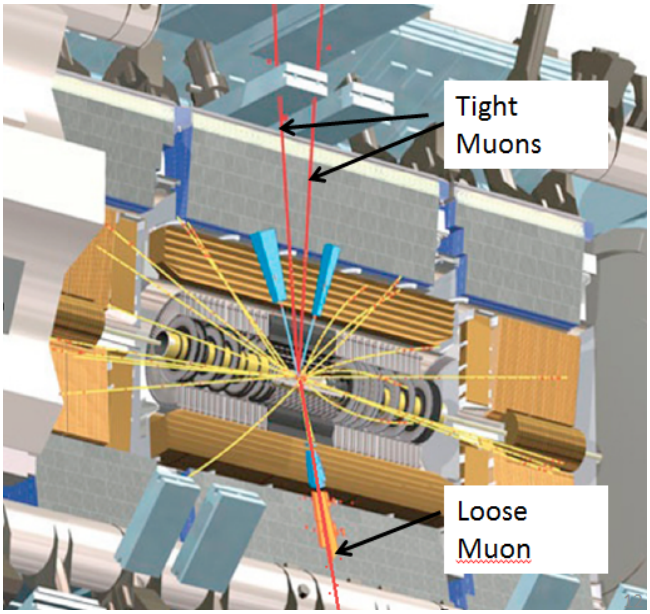

Figure 16: This cutaway of the ATLAS detector shows several tracks along with three muons tracks, which are show in red. The *loose* muon is graphically shown to have energy deposited in the calorimeter around its trajectory, as opposed to the *tight* muons that have deposited very little energy in the calorimeter.

At the heart of the fake matrix method is the Equation 2.1, where r and f denote real efficiency and fake rate, respectively. The subscripts, 1 and 2 denote leading p_T muon and sub-leading muon, respectively. This matrix relates the numbers of events with tight-tight (TT), tight-loose (TL), loose-tight (LT), and loose-loose (LL) lepton pairs that pass analysis

selection criteria (N_{TT} , N_{TL}, N_{LT} , N_{LL}) to the numbers of events with real-real (RR), real-fake (RF), fake-real (FR), and fake-fake (FF) lepton pairs that pass analysis selection criteria (N_{RR}, N_{RF}, N_{FR}, N_{FF}).

The 4×4 matrix in the equation 2.1 is constructed in the following manner: The observed number of TT events comes from RR, RF, FR and FF events in nature. The RR events are reconstructed as TT with an efficiency of $r_1 \cdot r_2$. The RF events are constructed as TT with an efficiency of $r_1 \cdot f_2$. Similarly the unfolding of real/fake pairs into tight/loose pairs are calculated by considering the appropriate efficiency factors, which are products of probabilities, r and f.

$$\begin{pmatrix} N_{\mathrm{TT}} \\ N_{\mathrm{TL}} \\ N_{\mathrm{LT}} \\ N_{\mathrm{LL}} \end{pmatrix} = M \begin{pmatrix} N_{\mathrm{RR}} \\ N_{\mathrm{RF}} \\ N_{\mathrm{FR}} \\ N_{\mathrm{FF}} \end{pmatrix} \tag{2.1}$$

where

$$M = \begin{pmatrix} r_1 r_2 & r_1 f_2 & f_1 r_2 & f_1 f_2 \\ r_1(1-r_2) & r_1(1-f_2) & f_1(1-r_2) & f_1(1-f_2) \\ (1-r_1)r_2 & (1-r_1)f_2 & (1-f_1)r_2 & (1-f_1)f_2 \\ (1-r_1)(1-r_2) & (1-r_1)(1-f_2) & (1-f_1)(1-r_2) & (1-f_1)(1-f_2) \end{pmatrix} \tag{2.2}$$

The goal of the fake matrix method is to estimate the number of events with fake leptons which are reconstructed as tight-tight muon pairs (therefore passing our nominal selection criteria), as shown in in Eq. 2.3.

$$N_{fake\to TT} = N_{RF\to TT} + N_{FR\to TT} + N_{FF\to TT} \tag{2.3}$$

Taking the inverse of Eq. 2.1 and solving for 2.3 yields Eq. 2.4.

$$\begin{pmatrix} N_{\mathrm{RF,FR}\to\mathrm{TT}} \\ N_{\mathrm{FF}\to\mathrm{TT}} \end{pmatrix} = \frac{1}{(r_1-f_1)(r_2-f_2)} \begin{pmatrix} -r_1(1-f_1)(1-r_2)f_2-(1-r_1)f_1r_2(1-f_2) & (1-r_1)f_1(1-r_2)f_2 \\ (f_1+r_1-2f_1r_1)r_2f_2 & -(1-r_1)f_1r_2f_2 \\ r_1f_1(f_2+r_2-2f_2r_2) & -r_1f_1(1-r_2)f_2 \\ -2r_1f_1r_2f_2 & r_1f_1r_2f_2 \end{pmatrix}^T \cdot \begin{pmatrix} N_{\mathrm{TT}} \\ N_{\mathrm{TL}} \\ N_{\mathrm{LT}} \\ N_{\mathrm{LL}} \end{pmatrix} \tag{2.4}$$

This equation is used to calculate the weight associated with an individual event. These weights are then summed over all events to estimate the QCD background. In order to perform such estimate, the real efficiencies and fake rates are first needed. Estimation of these quantities are described in section 2.5.1 below.

2.5.1 Measuring Real Efficiencies and Fake Rates

Real efficiencies and fake rates are estimated in bins of P_T and $\Delta\ R_{\mu,jet}$.

2.5.1.1 Real Efficiencies Real efficiencies are estimated using the *real control region*, which, by design, contains almost entirely *real* muons. We impose the following selection criteria on the events which satisfies the criteria described in section 2.4.

- The invariant mass of two muons should be within a narrow mass window [86,96] GeV around the Z peak.
- Two muons are required to be of opposite charges.
- All analysis selection criteria are applied except for the muon isolation criteria.

The measurement of real efficiency is performed using the tag and probe method. Tag is a loose muon (satisfying or failing the isolation criteria) which is required to have triggered the event. The probe is a tight muon (satisfying the isolation criteria) which is also required to have triggered the event. We use all both muons as the probe alternatively, and hence utilize all available statistics. This method is described below.

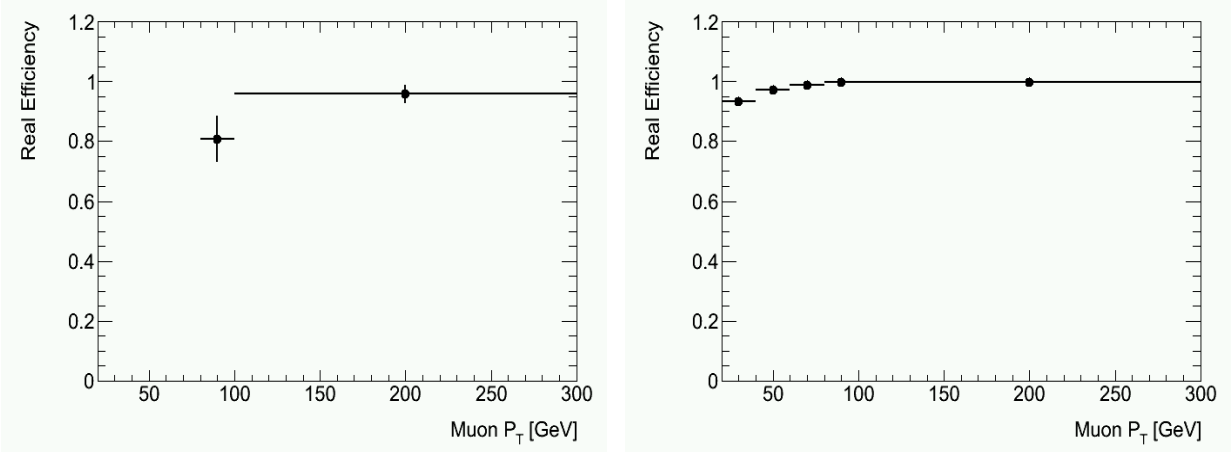

(a) (b)

Figure 17: Real efficiencies estimated from data. Figure on the left shows the real efficiency for muons close to jets, parameterized in P_T. The figure on the right shows real efficiency for muons that have no nearby jets, parameterized in P_T.

Four histograms, binned in kinematic variables of probes are prepared: h_1^{T}, h_1^{L}, h_2^{T} and h_2^{L}. When the first muon is selected as the tag, the second lepton is added to h_2^{T} or h_2^{L} respectively, depending on whether the second lepton is tight or loose. Similarly, when the second muon is selected as the tag, the first lepton is added to h_1^{T} or h_1^{L} respectively, depending on whether the first lepton is tight or loose. The efficiency is then estimated as $\epsilon = (h_1^{\mathrm{T}} + h_2^{\mathrm{T}})/(h_1^{\mathrm{T}} + h_1^{\mathrm{L}} + h_2^{\mathrm{T}} + h_2^{\mathrm{L}})$ The estimated real efficiencies are shown in Fig. 17.

2.5.1.2 Fake Rates Fake rates are estimated using the *fake control region*, which, by design, contains almost entirely *fake* muons. Two fake control regions are used to measure the fake rates. *Fake control region A* is used to measure the fake rates for those muons found well separated from jets. *Fake control region B* is used to measure the fake rates for muons which are found close to jets.

The selection criteria imposed to construct *fake control region A* include

- All object and event selection criteria, except for the muon isolation criteria are applied.
- Selecting only the same-sign dimuon events.
- Considering a region orthogonal to the signal regions by imposing cutoff $M(\mu\mu j(j)) < 400$ GeV.

The selection criteria imposed to construct *fake control region B* include

- Events with exactly 1 muon candidate are selected.
- To minimize W contamination, the transverse mass, evaluated using the missing transverse momentum and the muon, is required to satisfy $W_\perp < 40$ GeV, where $W_\perp = \sqrt{2E_{\mathrm{T}}^{\mathrm{Miss}} P_{\mathrm{T}\mu}(1 - \cos(\Delta\phi(\mu, E_{\mathrm{T}}^{\mathrm{Miss}})))}$.
- At least 1 analysis jet is required to be present.
- To further reduce W contamination, the angular separation between a muon and missing E_T is required to be less than 0.5 in the ϕ direction, $|\Delta\phi\left(E_T^{missing}, \mu\right)| < 0.5$
- The muon is required to have triggered the event.

To further reduce contamination of real muons in fake control region B, from W+jets, MC samples are used to subtract the contamination from the fake control region. The measurement of fake rate in control region A, tag and probe method is used similar to as explained in section 2.5.1.1. The measurement of fake rate in control region B is done by taking the ratio between tight muons and loose muons in the fake control region. The estimated fake rate is shown in Fig. 18.

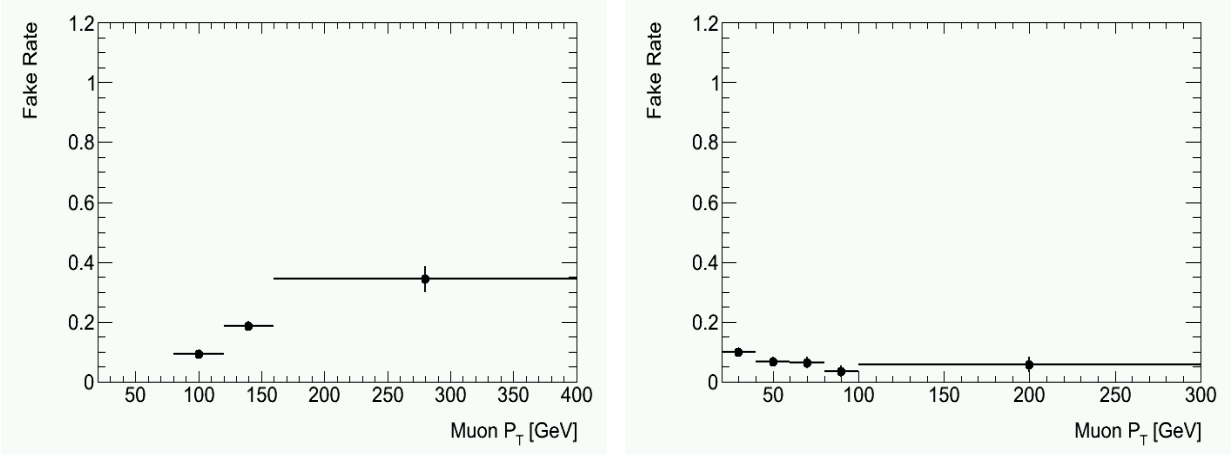

(a) (b)

Figure 18: Estimated fake rate for muons. Figure on the left shows the fake rate for muons close to jets, parameterized in P_T. The figure on the right shows fake rate for muons that have no nearby jets, parameterized in P_T.

3.0 SYSTEMATIC UNCERTAINTIES

3.1 SOURCES OF SYSTEMATIC UNCERTAINTIES

Depending on their sources, the systematic uncertainties of our measurement could be separated into several groups. The first group contains uncertainties associated with object reconstruction. The second group contains trigger efficiency uncertainties. Modeling the hard processes and hadronization comprise the third group. We discuss these systematic uncertainties and their sources below.

3.1.1 Jet Energy Scale and Resolution

Since the start of beam collisions in 2010 at the LHC, the instantaneous luminosity has increased dramatically. The higher luminosity was achieved by increasing the number of protons per bunch and the number of bunches per train in the proton beams. Number of bunches per beam have gone up from 50 in 2010 to 1380 in 2011. [56]

All MC simulation samples are generated with multiple pp interactions per bunch crossing (pile-up). Thus the number of average interactions per beam crossing is a data taking period dependent quantity, which is, by design, different from the one implemented in MC samples that were generated before the data were recorded. These simulated events are re-weighted so that the distribution of the number of interactions per crossing in simulation matches that in the data.

Producing new MC samples of necessary size, especially for backgrounds, is unrealistic, Therefore we use existing MC samples to provide the estimates of overall detection efficiency, which depends on the average interactions per event (pile-up). Using MC samples

with wrong pile-up requires additional MC corrections, as the energies accumulated in the calorimeter depend on the amount pile-up, which depends on instantaneous luminosity of the LHC and its train-bunch structure. In particular, energies of hadronic jets in MC need to be corrected to match the data in a data taking period dependent way. Also, there are systematic uncertainties associated with these corrections, as they are derived using finite statistics and are subject to certain assumptions and a number of unknown factors.

There are two types of uncertainties associated with such corrections. These are the uncertainties associated with the **jet energy resolution** [59] and **jet energy scale** [60]. Software tools, *MultijetJESUncertaintyProvider* and *JetEnergyResolutionProvider*, provided by Jet/$E_{\mathrm{T}}^{\mathrm{Miss}}$ performance group were used to evaluate these uncertainties [57].

3.1.2 Muon Reconstruction

It was found that MC underestimates muon momentum transverse resolution. This discrepancy between data and MC is corrected by applying a smearing correction to the muons' transverse momenta. The systematic uncertainty associated with this **muon energy scale and resolution** correction was evaluated using standard ATLAS software tool, *MuonMomentumCorrections*. [47]

The uncertainties associates with the muon reconstruction and identification were also evaluated using standard ATLAS software tool, *MuonEfficiencyCorrections*. [48]

3.1.3 Single Muon Trigger

Single muon trigger efficiency measured from data differs from its MC predictions. As our signal event candidates contain two muons, this is a small effect which, nevertheless, must be taken into account. In principle, we could have used our own data trigger efficiency measurements for our analysis, however, for practical reasons (as it is required by the Collaboration) it is more convenient to account for this difference between MC and data by weighting MC events according to signal muon candidates kinematics.

A standard software tool *TrigMuonEfficiency* provided by the ATLAS combined muon performance group was used to evaluate the weights. The trigger scaling factor per event,

SF, is calculated according the the formula given in Eq. 3.1, where the product is taken over both leptons l in the event. In this formula ϵ is the single lepton trigger efficiency which depends on lepton's kinematics.

$$SF = \frac{1 - \prod \left(1 - \epsilon_l^{MC}\right)}{1 - \prod \left(1 - \epsilon_l^{Data}\right)} \tag{3.1}$$

3.1.4 Summary of Reconstruction Sourced Systematic Uncertainties

The Table 2 and Table 3 shows the breakdown of the systematic uncertainties summarized in Table 4 and Table 5, which shows the overall systematic uncertainties for each SM background category.

	Z+jets	Diboson	ttbar	single top
Events	1532.54	61.20	658.67	50.67
JER	0.04	0.04	0.00	0.02
JES↑	0.13	0.07	0.04	0.05
JES↓	0.30	0.07	0.05	0.06
ID↑	0.04	0.01	0	0
ID↓	0.05	0.01	0	0
MS↑	0.18	0.05	0	0
MS↓	0.28	0.06	0	0
MU Eff	0	0	0	0
MU Trig	0	0	0	0

Table 2: Summary of the systematic uncertainties associated with MC background predictions for events with opposite-sign muon pairs. Baseline selection criteria are applied as well as background suppression criteria $M(\mu\mu) > 110\ GeV$ and $M(\mu\mu j(j) > 400\ GeV)$. The numbers of events are normalized to integrated pp luminosity of 4.7 fb^{-1}. The uncertainties are shown as relative fractions. ↑ and ↓ indicate the asymmetric uncertainties.

	Z+jets	Diboson	ttbar	single top
Events	0.12	2.43	0.93	0.12
JER	0	0.04	0	0
JES↑	0	0.16	0	0
JES↓	0	0.08	0.03	0
ID↑	0	0.00	0.03	0
ID↓	0	0.01	0	0
MS↑	0	0.01	0.03	0
MS↓	0	0.02	0.03	0
MU Eff	0	0.00	0	0
MU Trig	0	0.00	0	0

Table 3: Summary of the systematic uncertainties associated with MC background predictions for events with same-sign muon pairs. Baseline selection criteria are applied as well as background suppression criteria $M(\mu\mu) > 110\ GeV$ and $M(\mu\mu j(j) > 400\ GeV)$. The numbers of events are normalized to integrated pp luminosity of 4.7 fb^{-1}. The uncertainties are shown as relative fractions. ↑ and ↓ indicate the asymmetric errors.

3.1.5 Parton Density Functions

The uncertainties in Parton Density Functions (PDFs) are propagated to the cross sections and acceptance. Furthermore, there are several different PDF sets available, *e.g.* CTEQ66 and NNPDF2.0. MC samples generated with different sets of PDFs predict different central values for acceptance, so there is a systematic uncertainty associated with PDF set as well as the uncertainty within the PDF set. To estimate systematic uncertainty associated with this source of uncertainty, we employed the PDF re-weighting technique.

PDF re-weighting was used to estimate the effect of PDF + α_S uncertainties on overall signal detection efficiency. LHAPDF libraries [49] were used for doing the re-weighting. The LRSM samples were produced using with MRST2007lomod [50] PDF set. Following the

recommendations from PDF4LHC group [51], the comparison of the results obtained using PDF sets MSTW08NLO, CTEQ66 and NNPDF2.0 was performed.

A representative pair of mass parameters, $M(W_R = 1500$ GeV and $M(N) = 800$ GeV was used in evaluating the uncertainties. The conclusion was drawn that PDF effect on acceptance for LRSM samples was 9%. The summary of the PDF re-weighting results is shown in Fig. 19.

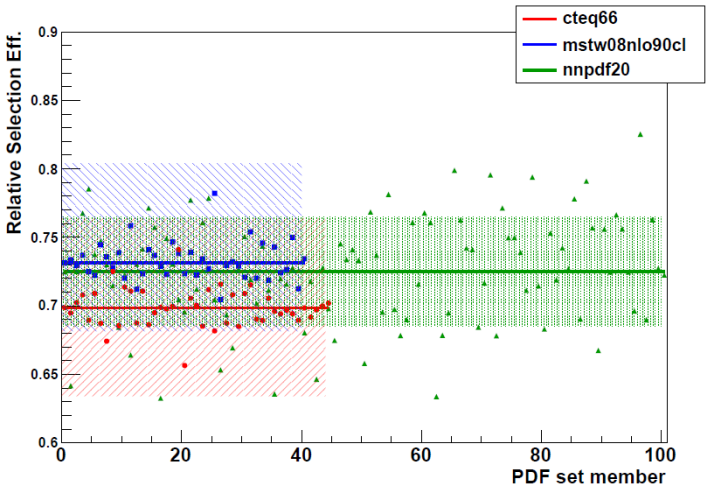

Figure 19: The summary of uncertainties in acceptance for the process $pp \to W_R(1500)X$ followed by decay $W_R(1500) \to lN_l(800)$ at pp invariant mass of 7 TeV for different sets of PDF shape parameters obtained with PDF sets MSTW2008nlo at 90%CL (blue), CTEQ66 (red), and NNPDF20 (green).

3.1.6 Integrated pp Luminosity

There are two primary detectors in ATLAS which are used to make bunch-by-bunch luminosity measurements: LUCID and BCM. LUCID is a Cerenkov detector specifically designed for measuring the luminosity in ATLAS. The Beam Conditions Monitor (BCM) consists of four small diamond sensors on each side of the ATLAS interaction point (IP) arranged around the beam-pipe in a cross pattern. The BCM is a fast device primarily designed to monitor background levels and issue a beam-abort request in case beam losses start to risk damage

to ATLAS detectors.

The luminosity and its systematic uncertainties are affected due to several processes. Variations in beam conditions such as position, jitter and emittance growth, instrumentation uncertainties and uncertainties in calibration affects the overall uncertainty in luminosity.

A relative luminosity uncertainty of $\Delta L/L = \pm 3.7\%$ is used following the recommendations by the ATLAS collaboration. More information could be found in the Ref. [58]

3.2 QCD BACKGROUND ESTIMATE AND HALF SAMPLE TEST

The (previously discussed) fake matrix method used for estimating the QCD background relies on the estimates of real efficiencies (r) and fake rates (f). Half Sample Test (HST) is a closure test, where we estimate the uncertainty associated with the parametrization of r and f.

The HST is carried out by splitting the data set into two sub-samples, each corresponding approximately to 2.35 fb^{-1} of integrated luminosity. Splitting is done by generating a random number to determine which event falls into which sub-sample. The first half of the data is used to measure the real efficiencies and fake rates, which are denoted by $r_{1,\mathrm{m}}$ and $f_{1,\mathrm{m}}$. The real efficiencies and fake rates are also measured using the second half of the data and are denoted by $r_{2,\mathrm{m}}$ and $f_{2,\mathrm{m}}$. Then, $r_{1,\mathrm{m}}$ and $f_{1,\mathrm{m}}$ are used to predict the real efficiencies and fake rates, which are denoted by $r_{2,\mathrm{p}}$ and $f_{2,\mathrm{p}}$. We use a comparison between the predicted and measured rates to assign an uncertainty to the r's and f's, where the measured values r and f are evaluated as described in section 2.5.1. Evaluation and definition of the predicted quantities $r_{2,\mathrm{p}}$ and $f_{2,\mathrm{p}}$ are described below.

Suppose the second half of the sample consists of N^{L} number of loose leptons, which could be either real leptons or fake leptons. This sample is represented in Eq. 3.2. Out of the N^{L} number of *loose* leptons, N^{T} number of leptons are reconstructed as *tight*, satisfying the isolation criteria (defined in section 2.3.1). Contributions to N^{T} are shown in Eq. 3.3. Inverting Equations 3.2 and 3.3 yields Equations 3.4 and 3.5.

$$N^{\mathrm{L}} = N^{\mathrm{L}}_{\mathrm{R}} + N^{\mathrm{L}}_{\mathrm{F}} \tag{3.2}$$

$$N^{\mathrm{T}} = rN_{\mathrm{R}}^{\mathrm{L}} + fN_{\mathrm{F}}^{\mathrm{L}} \tag{3.3}$$

$$N_{\mathrm{R}}^{\mathrm{L}} = \frac{1}{r-f}\left(N^{\mathrm{T}} - fN^{\mathrm{L}}\right) \tag{3.4}$$

$$N_{\mathrm{F}}^{\mathrm{L}} = \frac{1}{r-f}\left(rN^{\mathrm{L}} - N^{\mathrm{T}}\right) \tag{3.5}$$

The predicted real efficiency $r_{2,\mathrm{p}}$ is defined in Eq. 3.6, while the predicted fake rate is defined in Eq. 3.7.

$$r_{2,\mathrm{p}} = \frac{N_{predicted}^{\mathrm{T}}}{N^{\mathrm{L}}} = r_{1,\mathrm{m}}\frac{N_{\mathrm{R}}^{\mathrm{L}}}{N^{\mathrm{L}}} \tag{3.6}$$

$$f_{2,\mathrm{p}} = \frac{N_{predicted}^{\mathrm{T}}}{N^{\mathrm{L}}} = r_{1,\mathrm{m}}\frac{N_{\mathrm{F}}^{\mathrm{L}}}{N^{\mathrm{L}}} \tag{3.7}$$

Using expressions in Eq. 3.4 and Eq. 3.5 in Eq. 3.6 and Eq. 3.7, respectively, gives simplified expressions for $r_{2,\mathrm{p}}$ and $f_{2,\mathrm{p}}$.

$$r_{2,\mathrm{p}} = \frac{r_{1,\mathrm{m}}}{r_{1,\mathrm{m}} - f_{1,\mathrm{m}}}\left(r_{2,\mathrm{m}} - f_{1,\mathrm{m}}\right) \tag{3.8}$$

$$f_{2,\mathrm{p}} = \frac{f_{1,\mathrm{m}}}{r_{1,\mathrm{m}} - f_{1,\mathrm{m}}}\left(r_{1,\mathrm{m}} - f_{2,\mathrm{m}}\right) \tag{3.9}$$

The relative differences between the measured and the predicted values for r and f are used as the estimates of systematic uncertainties for these quantities. Thus estimated uncertainties in the real efficiencies are shown in Fig. 20 and Fig. 21. The uncertainties in fake rates are shown in Fig. 22 and Fig. 23.

The QCD background may be estimated using the r and f estimated in section 2.5.1, and also using the adjusted r and f with uncertainties shown in Fig. 20, Fig. 21, Fig. 22 and Fig. 23. The difference between these two estimates of QCD is taken as the uncertainty on the QCD estimate, which are shown in the Table 4 (OS) and Table 5 (SS).

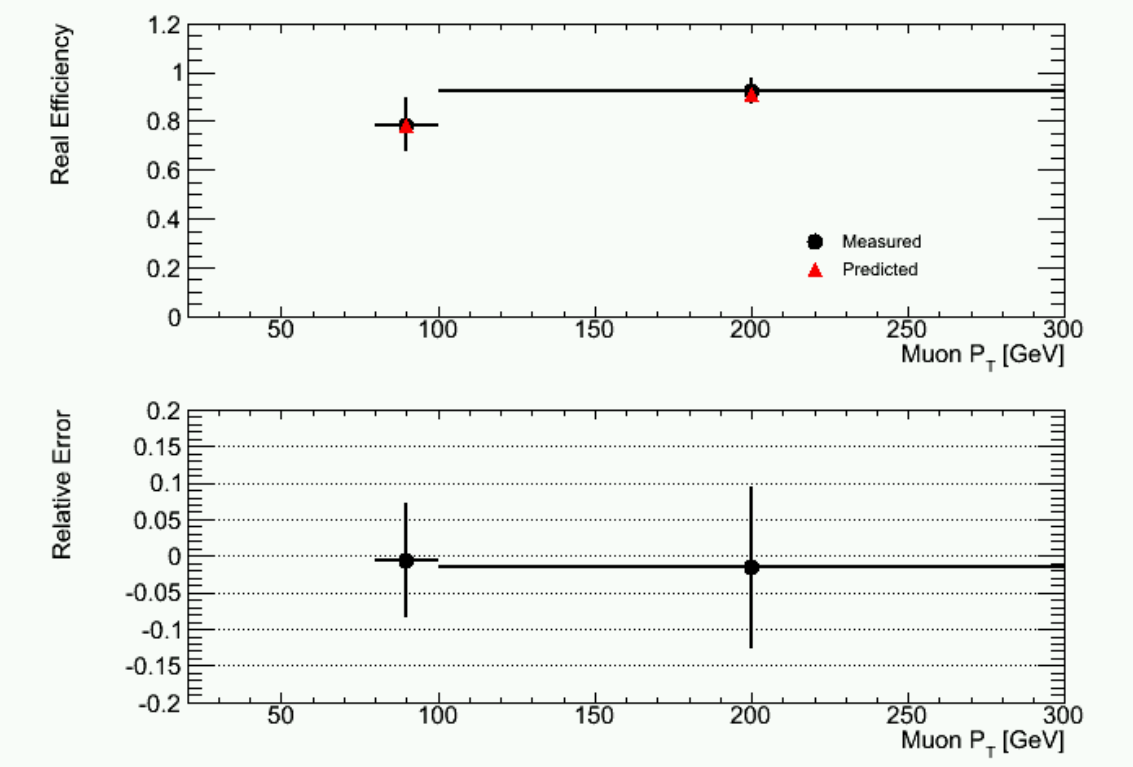

Figure 20: The uncertainty on r for muons found close to a jet estimated using the HST method. The top plot shows a comparison between the measured and the predicted values for real efficiencies. The bottom plot shows the relative difference between the predicted and the measured values., *i.e.* our estimate of the systematic uncertainty in r.

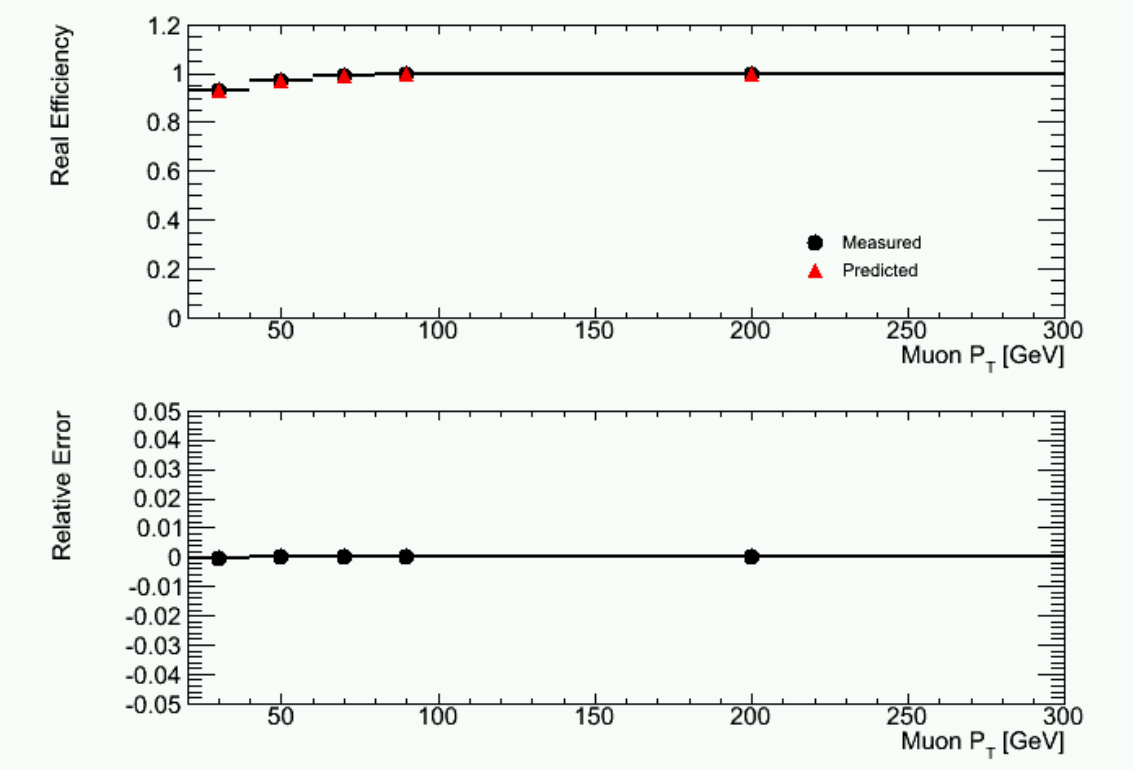

Figure 21: The uncertainty on r for muons well separated from jets estimated using the HST method is estimated by considering relative difference between measured and predicted values of r.The top plot shows a comparison between the measured and the predicted values for real efficiencies. The bottom plot shows the relative difference between the predicted and the measured values.

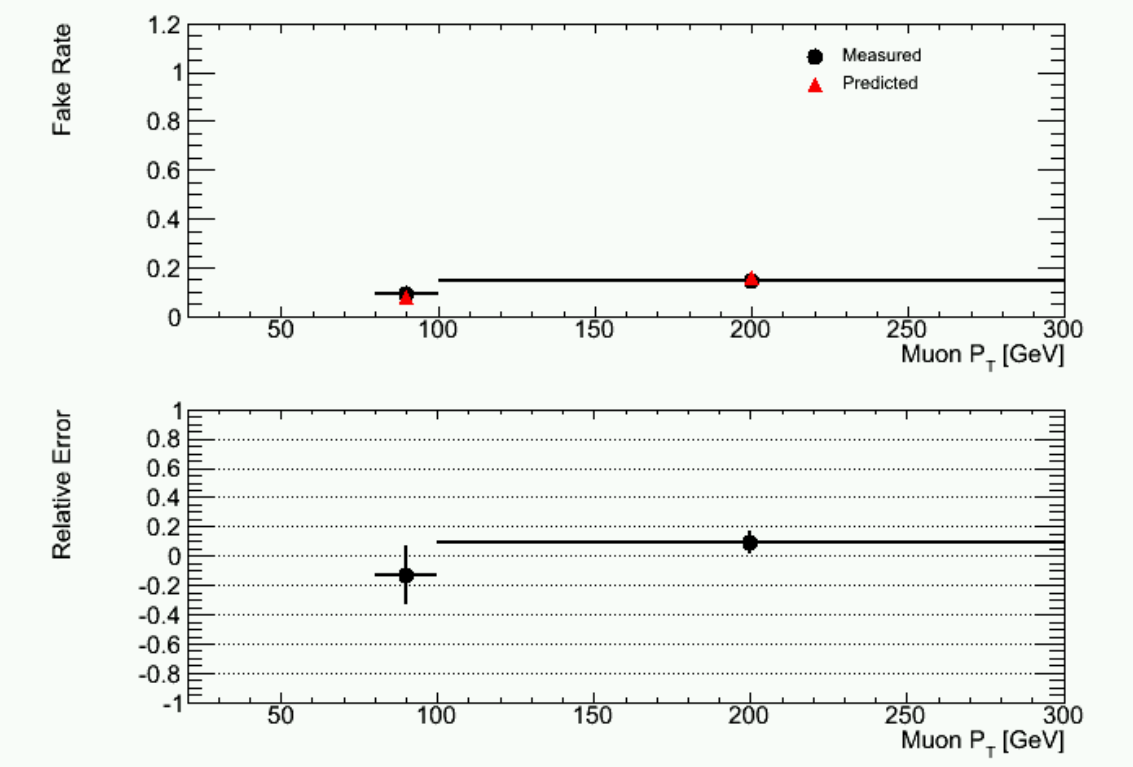

Figure 22: The uncertainty on f for muons close to a jet estimated using the HST method. Top plot shows the comparison between the measured and the predicted values for fake rates. The botom plot shows the relative difference between the predicted and the measured values, *i.e.* our estimate of systematic uncertainty in f.

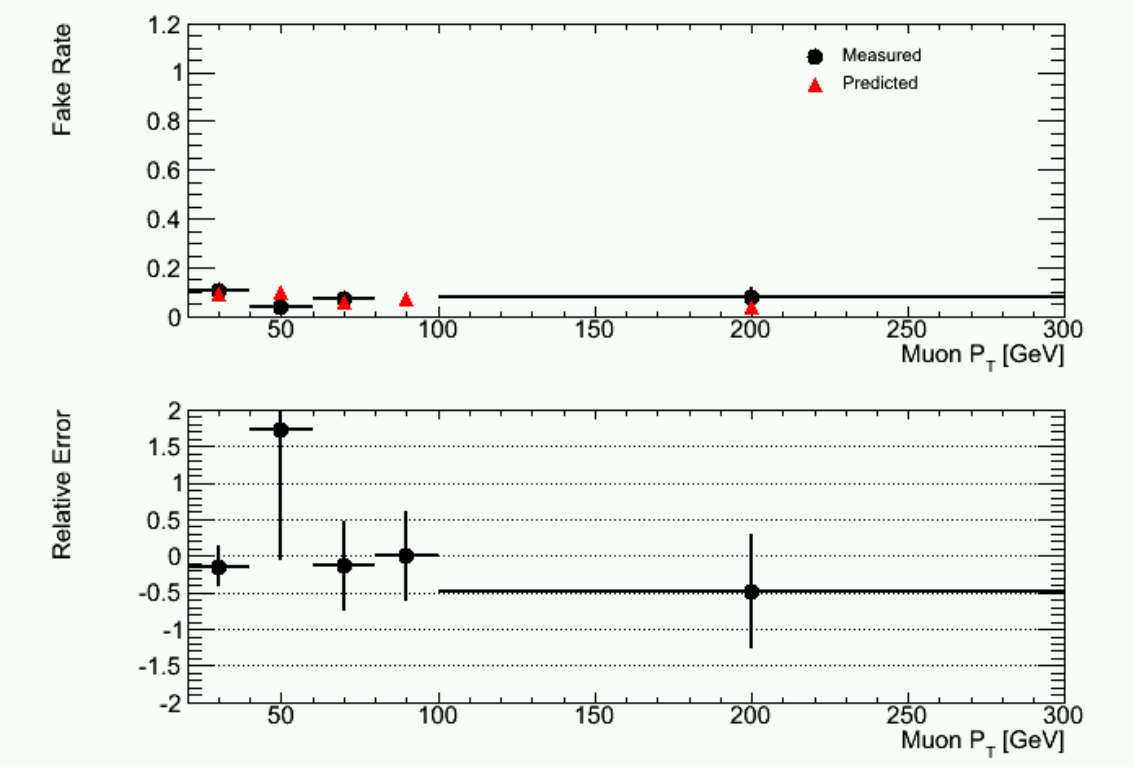

Figure 23: The uncertainty on f for muons not close to a jet estimated using the HST method. Top plot shows the comparison between the measured and the predicted values for fake rates. The botom plot shows the relative difference between the predicted and the measured values, *i.e.* our estimate of systematic uncertainty in f.

4.0 RESULTS

4.1 KINEMATIC DISTRIBUTIONS

The distributions of dimuon invariant mass, $M(\mu\mu)$, are shown in Fig. 24. The distributions of invariant mass of two muons and (up to) two jets, $M(\mu\mu j(j))$, are shown in Figures 25 to 28. The distributions of invariant mass of subleading P_T muon and (up to) two jets, $M(\mu j(j))$ are shown in Figures 29 to 32. Additional background suppression criteria applied to prepare plots shown in these figures are explained in Sec. 2.4.1.

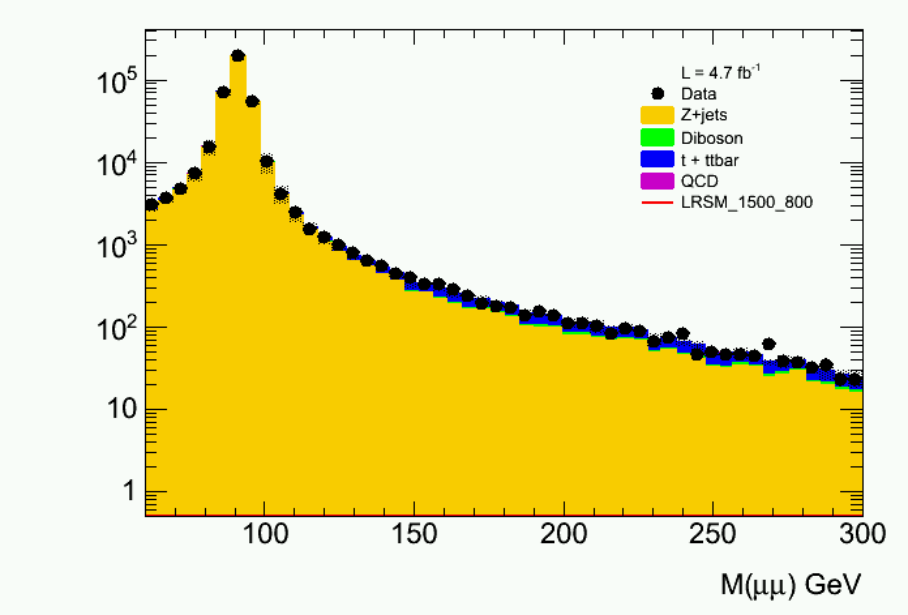

(a)

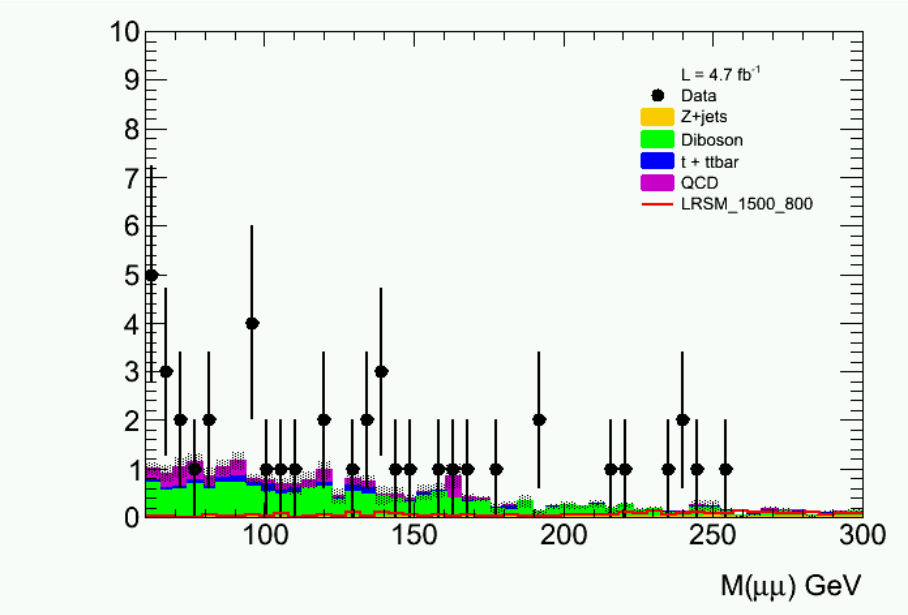

(b)

Figure 24: Distributions of dimuon mass for opposite-sign (top) and same-sign (bottom) dimuon pairs in data and MC simulation for SM backgrounds and a representative MC signal.

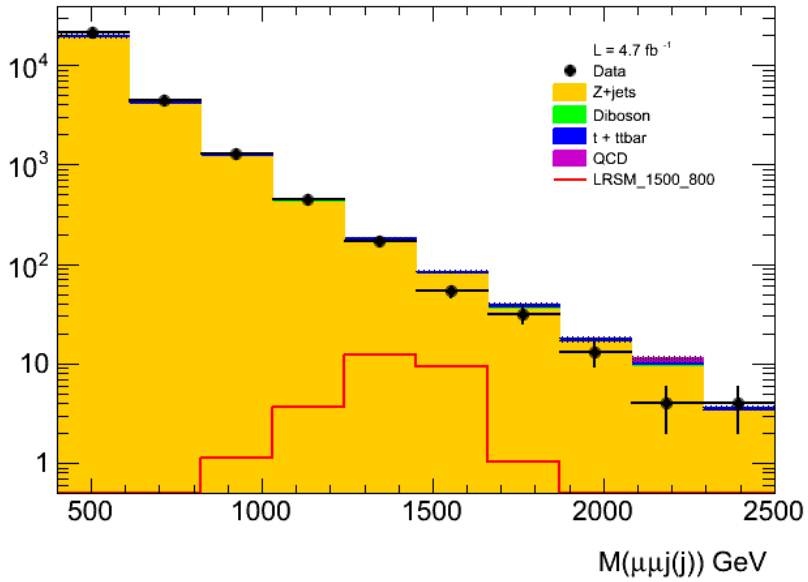

(a)

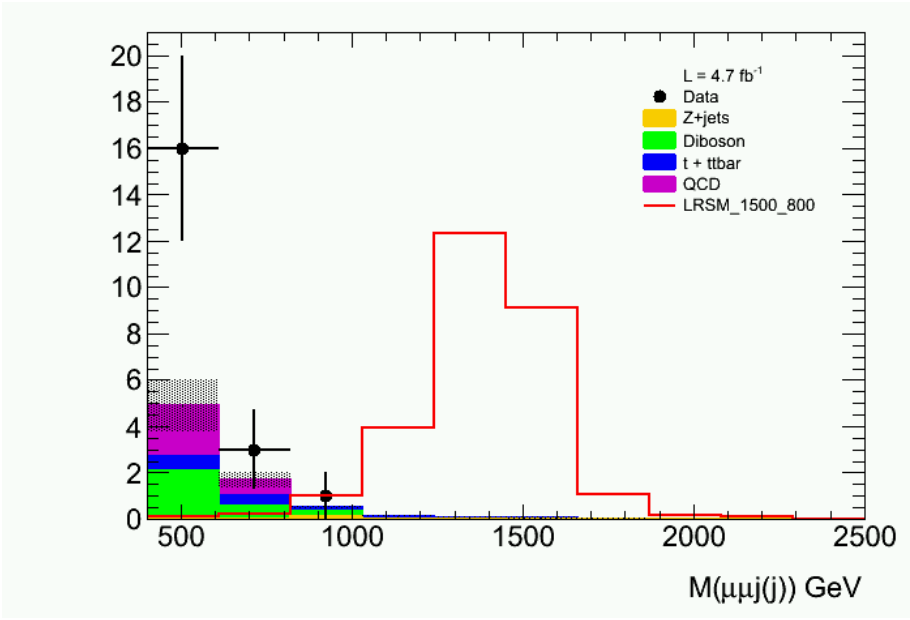

(b)

Figure 25: Distributions of $M(\mu\mu j(j))$ for opposite-sign (top) and same-sign (bottom) dimuon events.

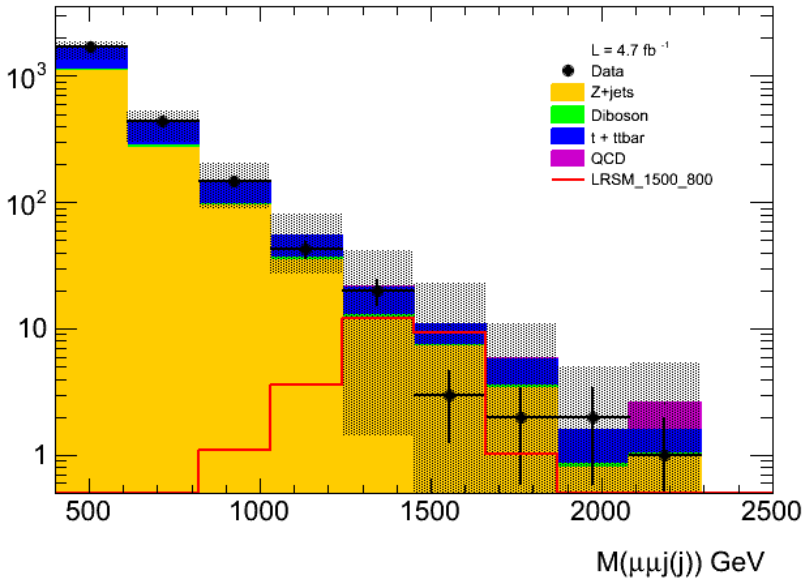

(a)

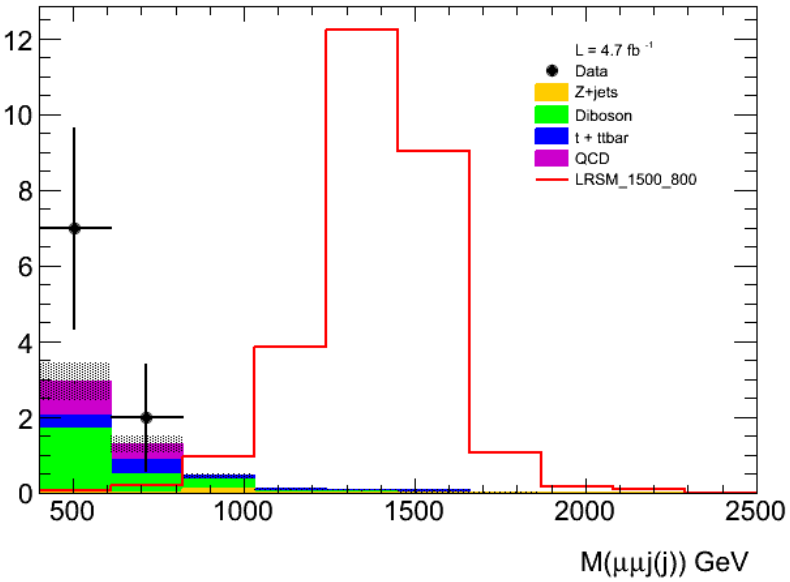

(b)

Figure 26: Distributions of $M(\mu\mu j(j))$ for opposite-sign (top) and same-sign (bottom) dimuon events. Additional background suppression criterion, $M(\mu\mu) > 110$ GeV is applied.

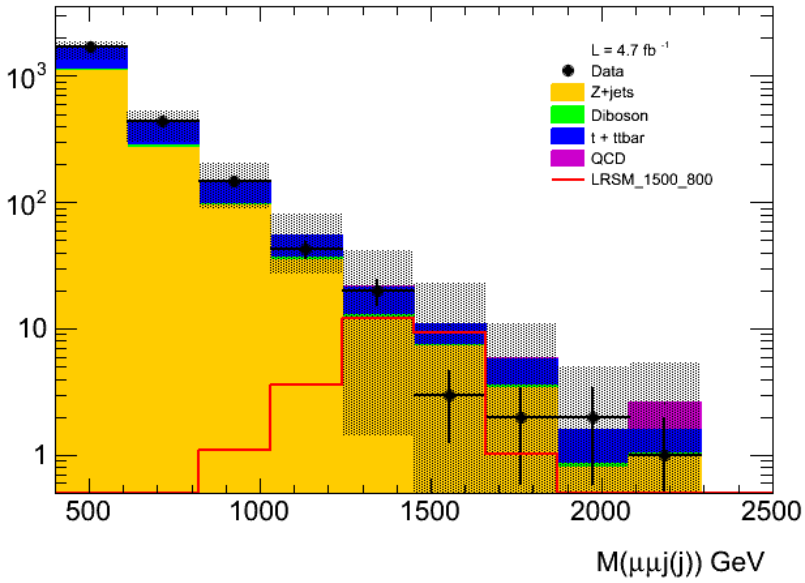

(a)

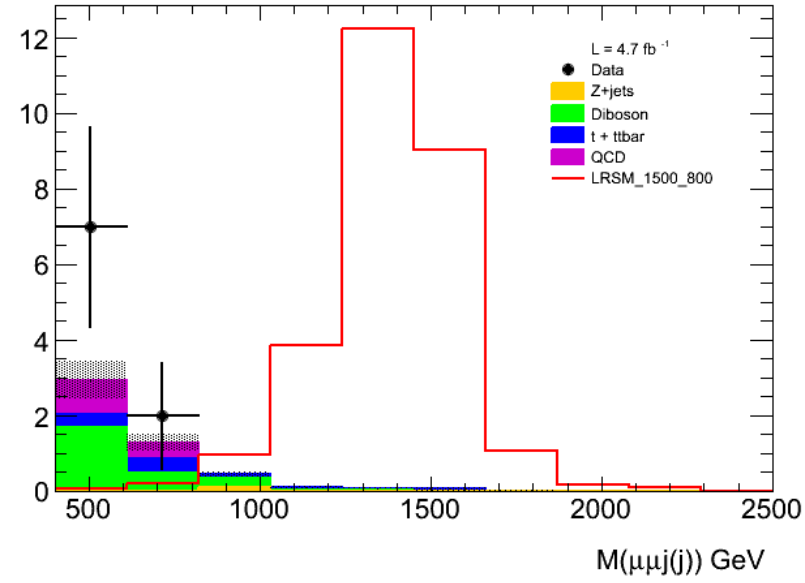

(b)

Figure 27: Distributions of $M(\mu\mu j(j))$ for opposite-sign (top) and same-sign (bottom) dimuon events. Additional background suppression criteria $M(\mu\mu) > 110$ GeV and $M(\mu\mu j(j)) > 400$ GeV are applied.

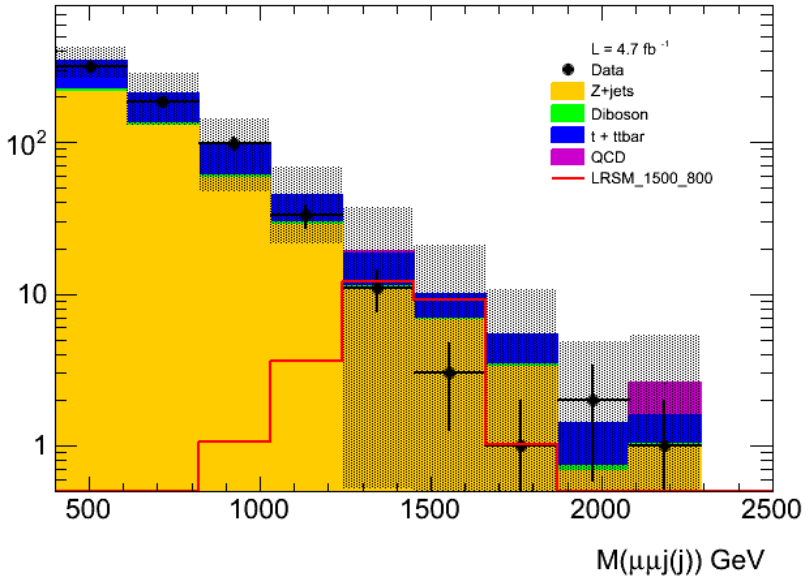

Figure 28: Distributions of $M(\mu\mu j(j))$ is shown for opposite-sign dimuon events. Additional background suppression criteria $M(\mu\mu) > 110$ GeV, $M(\mu\mu j(j)) > 400$ GeV and $S_T > 400$ GeV are applied.

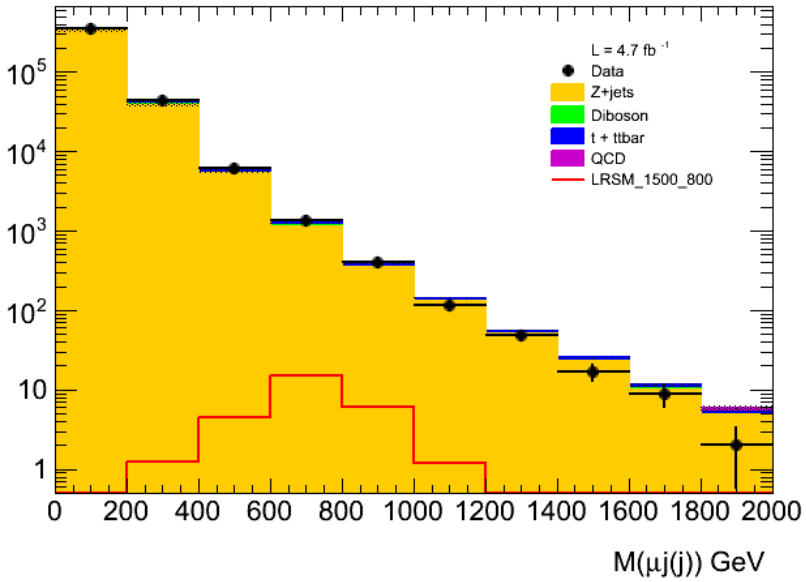

(a)

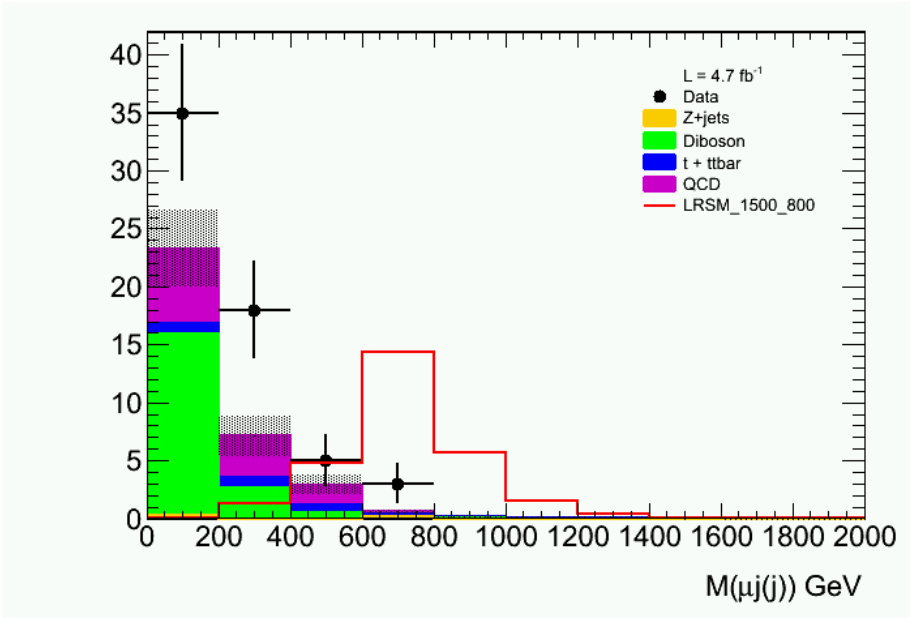

(b)

Figure 29: Distributions of $M(\mu j(j))$ for opposite-sign (top) and same-sign (bottom) dimuon events.

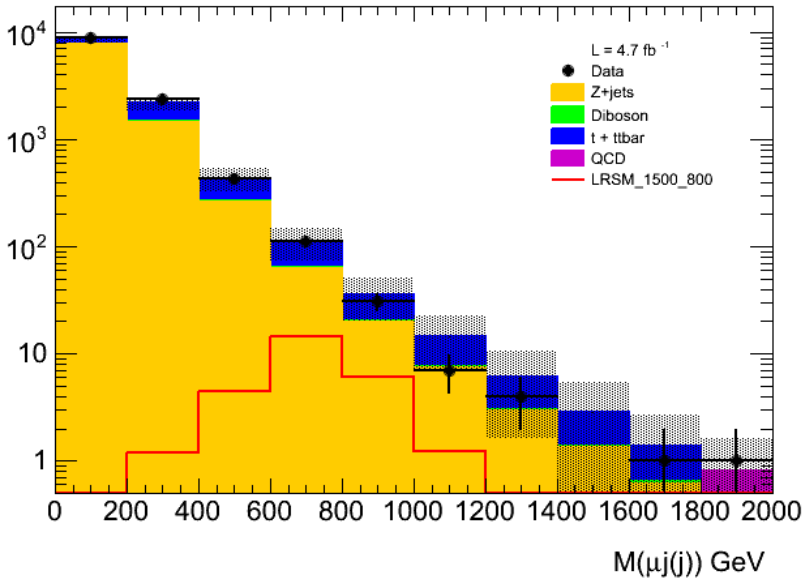

(a)

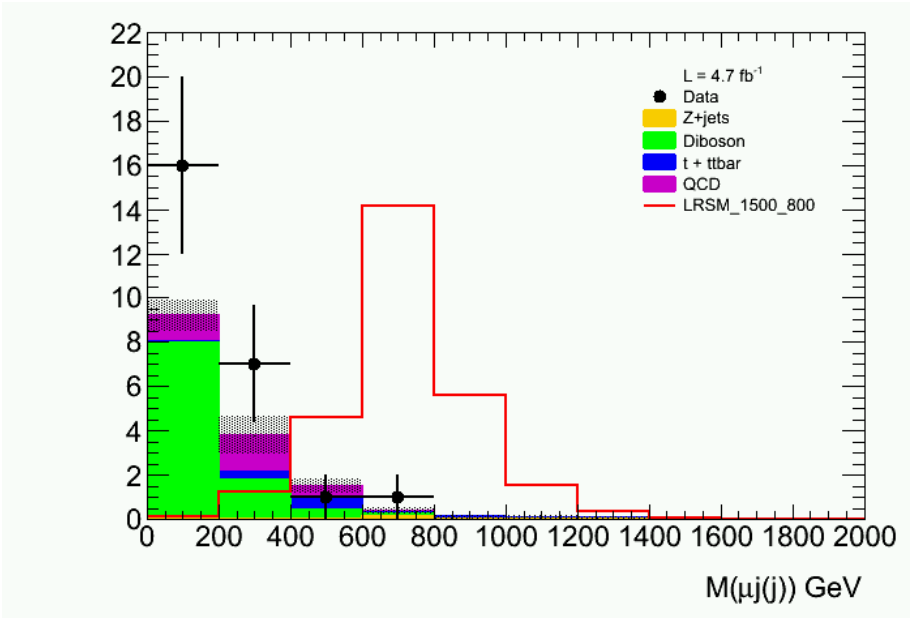

(b)

Figure 30: Distributions of $M(\mu j(j))$ for opposite-sign (top) and same-sign (bottom) dimuon events. Additional background suppression criterion, $M(\mu\mu) > 110$ GeV is applied.

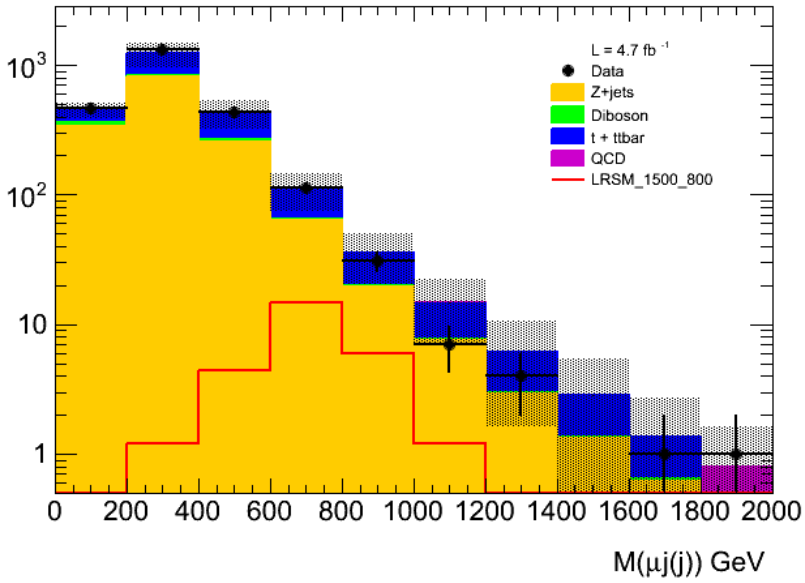

(a)

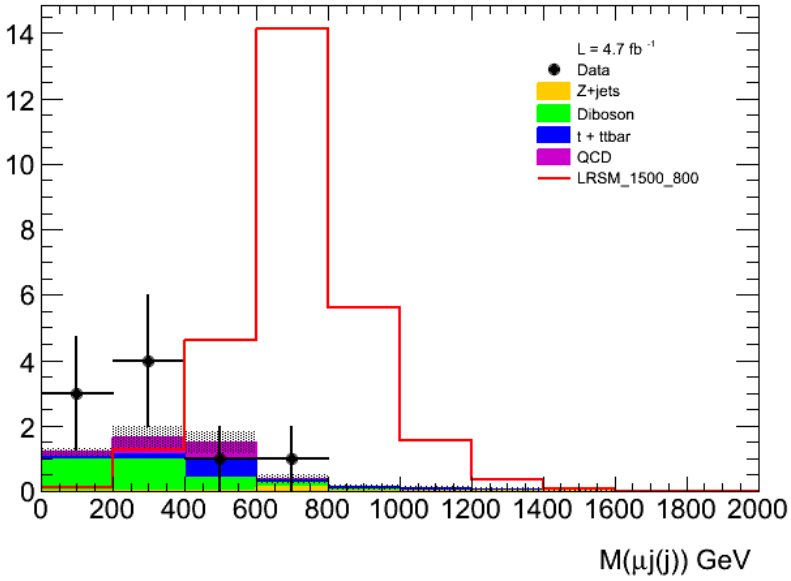

(b)

Figure 31: Distributions of $M(\mu j(j))$ for opposite-sign (top) and same-sign (bottom) dimuon events. Additional background suppression criteria $M(\mu\mu) > 110$ GeV and $M(\mu\mu j(j)) > 400$ GeV are applied.

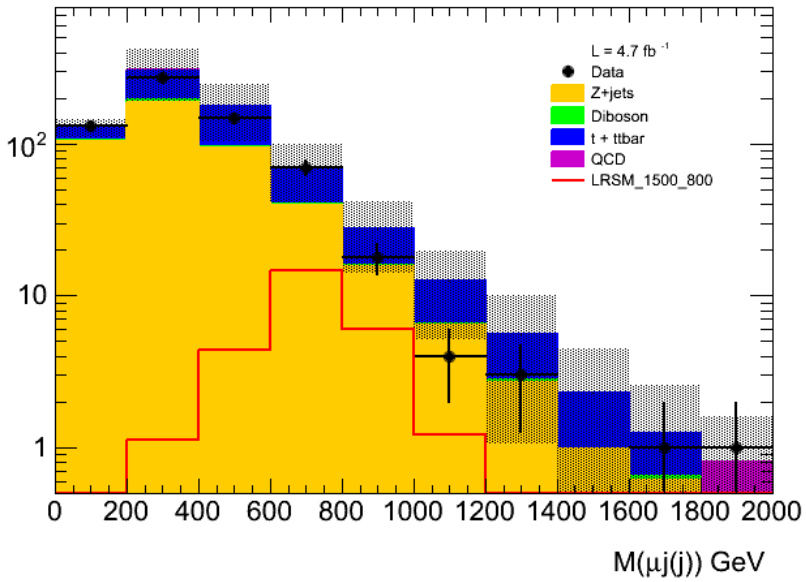

Figure 32: Distributions of $M(\mu j(j))$ is shown for opposite-sign dimuon events. Additional background suppression criteria $M(\mu\mu) > 110$ GeV, $M(\mu\mu j(j)) > 400$ GeV and $S_T > 400$ GeV are applied.

4.2 EVENT DISPLAYS

A small number of data events satisfy selection criteria we developed for our analysis. While the number of observed events in data is consistent with our estimates of SM backgrounds, each such event deserves an additional scrutiny, as it could be the first observation of some BSM process. In this section we describe some of the most interesting data events that are selected.

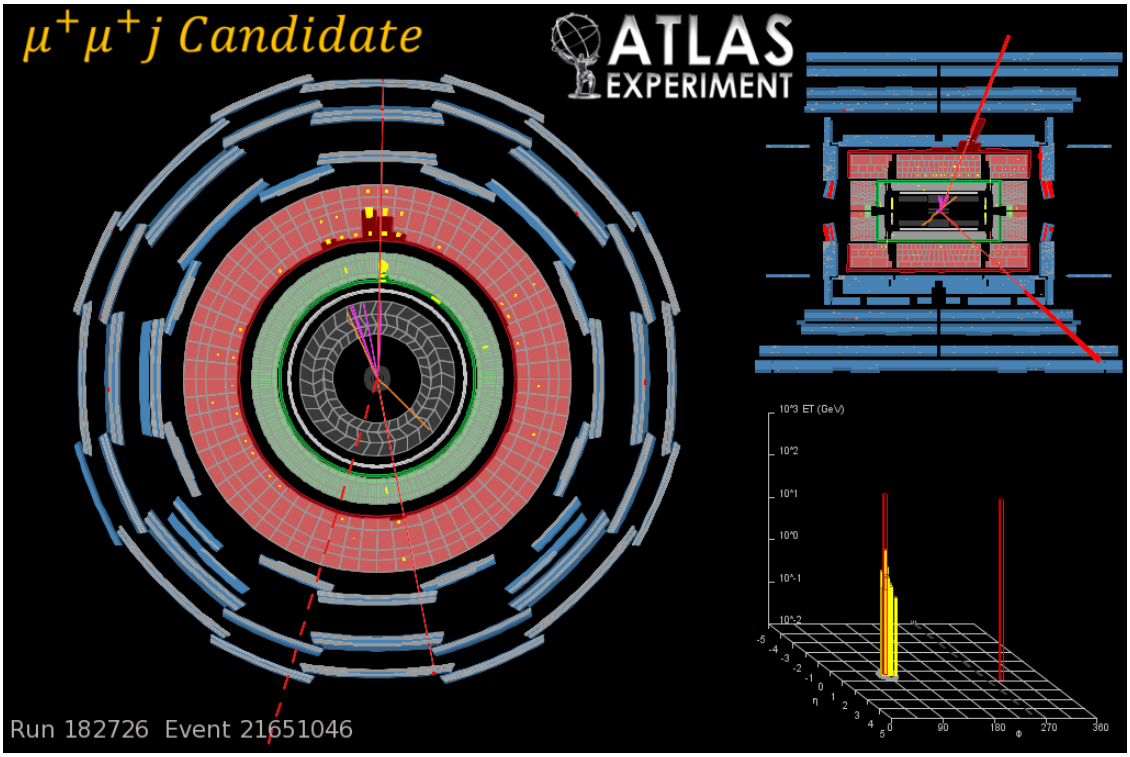

Figure 33: A same-sign dimuon+jet data event (Run number:182726, Event number: 21651046) that satisfies all selection criteria in our analysis. See the text for the detailed information about this data event.

Figure 33 shows an event display of a SS dimuon channel data event. The highest momentum muon has a p_{T} of 187 GeV and an (η, ϕ) of (-0.39,1.55). The subleading muon has a p_{T} of 183 GeV and an (η, ϕ) of (0.93,-1.38). The jet has p_{T} of 149 GeV and an (η, ϕ) of (0.46,1.59). The dimuon invariant mass is 383 GeV and $m_{lljj} = 512$ GeV. The left part

of the figure shows the view of the along the beam axis. Solid red lines represents the muon tracks. Inner detector tracks are represented by the line segments inside the inner detector. The broken red line represents missing transverse energy. Upper-right corner of the figure shows the side view of the detector. Lower-right part of the figure shows a histogram of the energy deposits in the $\eta - \phi$ plane.

It could be seen that the two muons are almost back-to-back in the transverse plane, and one of the muon is found inside a jet. It is more plausible that this event is from a QCD process.

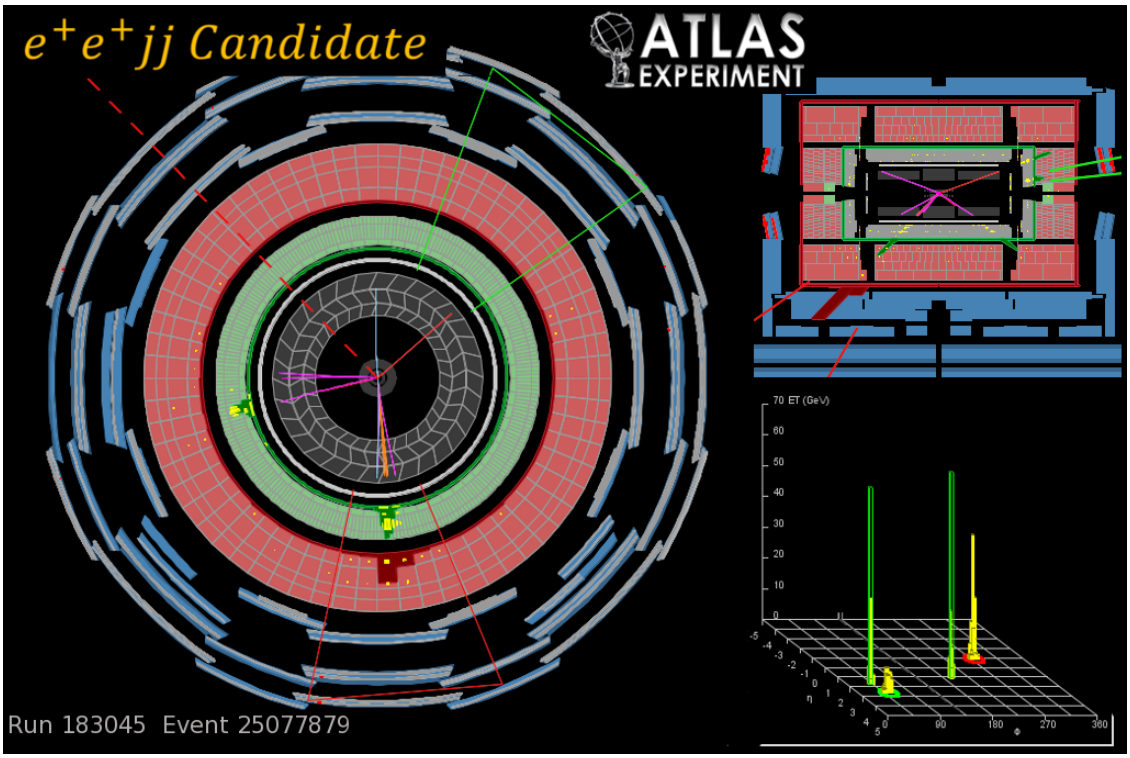

Figure 34: A same-sign dielectron+jet data event (Run number:183045, Event number: 25077879) that satisfies all selection criteria in our analysis. See the text for the detailed information about this data event.

Figure 34 shows an event display of a very high m_{ljj} data event found in the SS dielectron channel. The electrons are represented by the green histograms representing the energy deposits in the EM calorimeter (green circle). The highest momentum electron has a p_{T} of

67 GeV and an (η, ϕ) of (1.13,-2.9). The subleading electron has a p_{T} of 64 GeV and an (η, ϕ) of (1.73,0.72). The highest p_{T} jet has p_{T} of 235 GeV and an (η, ϕ) of (-0.86,-1.48). The subleading jet has p_{T} of 176 GeV and an (η, ϕ) of (2.63,0.92). The dielectron invariant mass is 133 GeV, $m_{lljj} = 1364$ GeV.

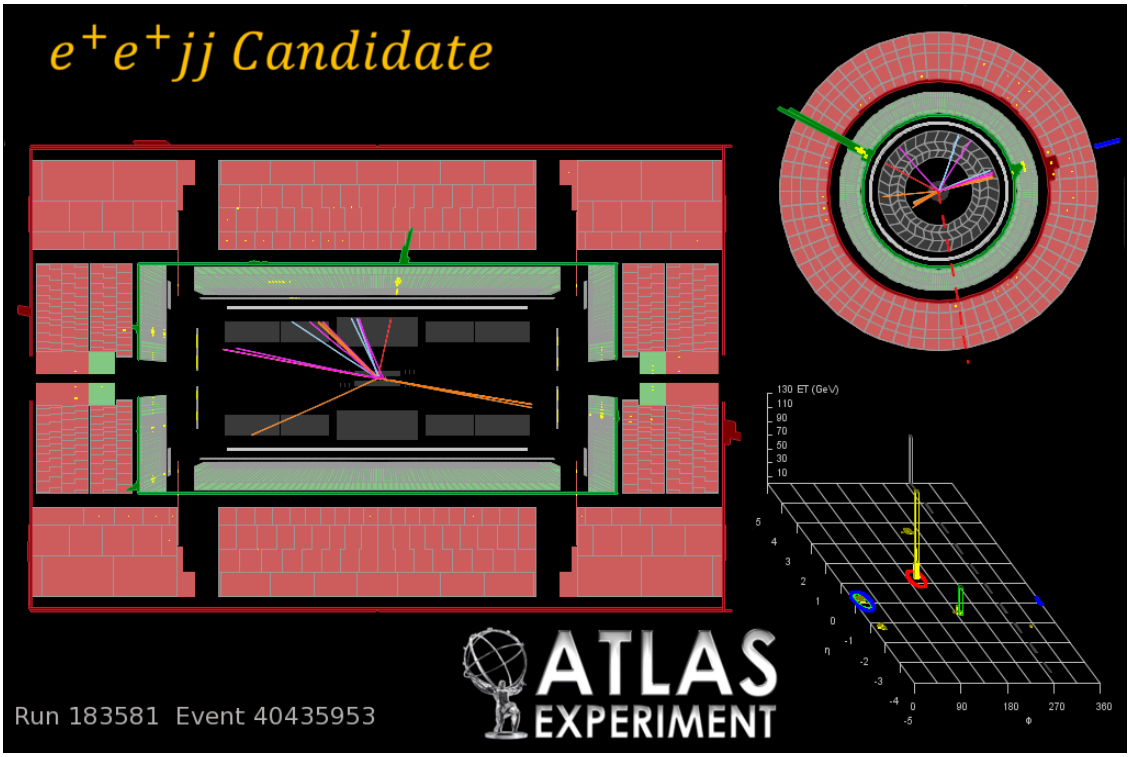

Figure 35: A same-sign dielectron+jet data event (Run number:183581, Event number: 40435953) that satisfies all selection criteria in our analysis. See the text for the detailed information about this data event.

Figure 35 shows an event display of a high m_{lljj} data event in the SS dielectron channel. The left side of the figure shows the side view of the detector. Upper-left part of the figure shows the view of the detector along the beam axis. The highest momentum electron has a p_{T} of 126 GeV and an (η, ϕ) of (0.21,2.67). The subleading electron has a p_{T} of 39 GeV and an (η, ϕ) of (-1.55,-3.02). The highest p_{T} jet has p_{T} of 121 GeV and an (η, ϕ) of (-0.89,0.28). The subleading jet has p_{T} of 96 GeV and an (η, ϕ) of (2.53,-2.66). The dielectron invariant mass is 147 GeV, $m_{lljj} = 906$ GeV.

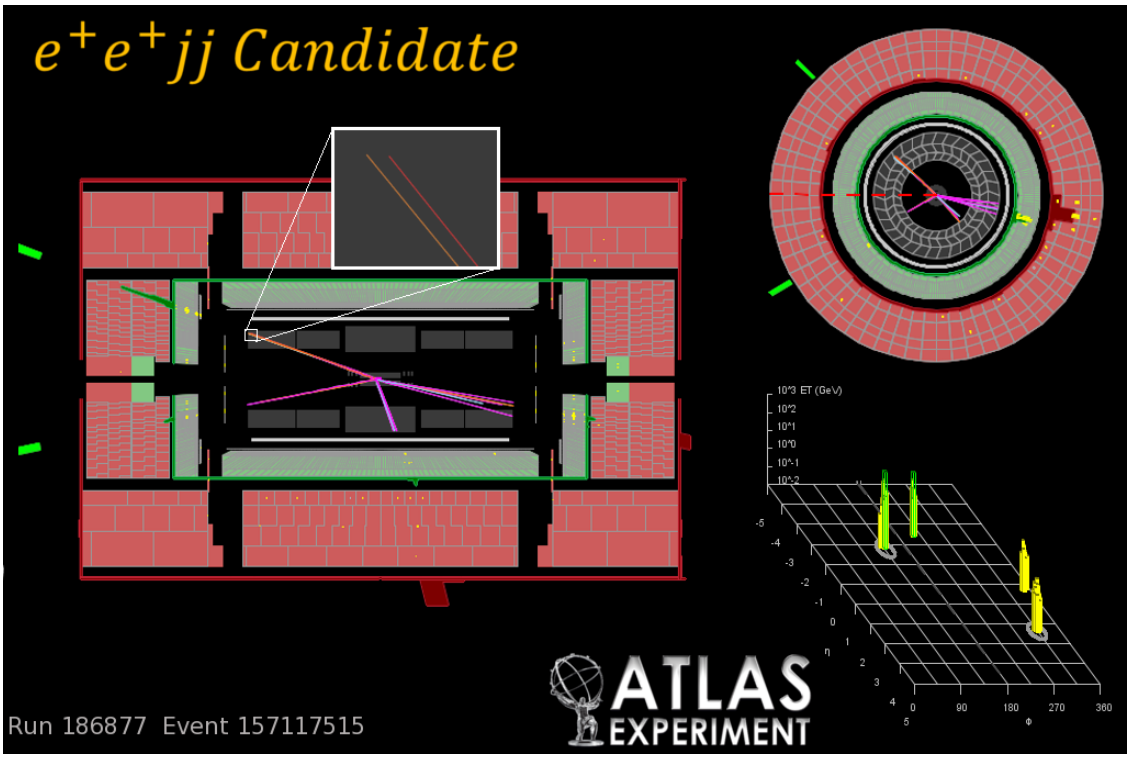

Figure 36: A same-sign dielectron+jet data event (Run number:186877, Event number: 157117515) that satisfies all selection criteria in our analysis. See the text for the detailed information about this data event.

Figure 36 shows an event display of a high m_{lljj} data event in the SS dielectron channel. In the side view of the detector, zooming in to a track associated with the electron shows that, it in fact consists of two tracks very close to each other. This is characteristic of a photo conversion having taken place. The same-sign of the electron pair may be attributed the charge mis-identification due to associating the "wrong" track with the electron energy cluster. The highest momentum electron has a p_{T} of 211 GeV and an (η, ϕ) of (-1.74,2.38). The insert shows that the leading electron is a conversion from a hard bremsstrahlung. The subleading electron has a p_{T} of 40 GeV and an (η, ϕ) of (-2.32,-2.60). The highest p_{T} jet has p_{T} of 122 GeV and an (η, ϕ) of (2.38,-0.828). The subleading jet has p_{T} of 102 GeV and an (η, ϕ) of (0.35,-0.24). The dielectron invariant mass is 124 GeV, $m_{lljj} = 1593$ GeV.

4.3 SUMMARY OF RESULTS

The target signal region of $M(\mu\mu j(j)) > 400$ GeV are shown in Fig. 37 (OS) and Fig. 38. The summary of the observed and predicted number of events are shown in Tables 4-5. The predicted background are normalized to the luminosity in data, 4.7 fb^{-1}. The overall uncertainty of the estimated background is shown as gray uncertainty bands.

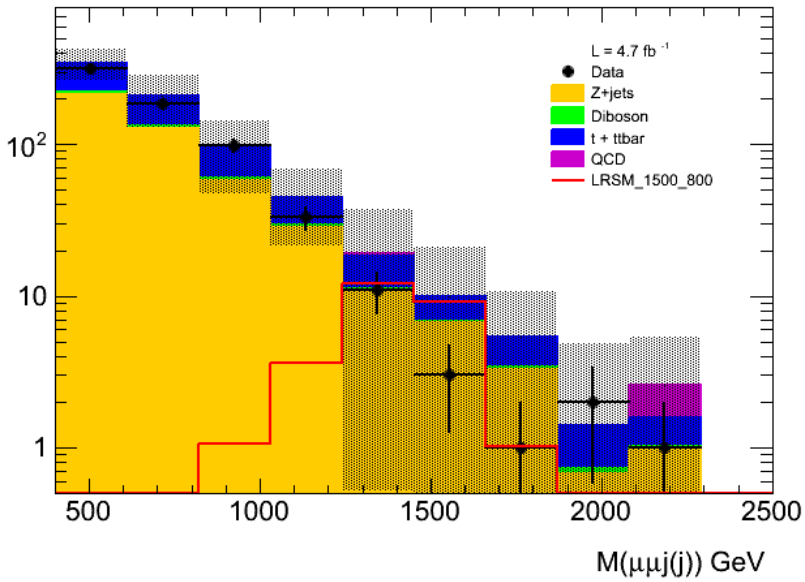

Figure 37: Distributions of $M(\mu\mu j(j))$ is shown for opposite-sign dimuon events. Additional background suppression criteria $M(\mu\mu) > 110$ GeV, $M(\mu\mu j(j)) > 400$ GeV and $S_T >$ 400 GeV are applied.

4.4 LIMITS ON W_R AND N MASSES

Based on the results presented in section 4.3, we set limits on production cross sections $\sigma(pp \to W_R)$. We use frequentist's approach to calculate the upper limits for exclusion at 95% confidence limits (CL). A RooFit-based framework for statistical data analysis called RooStats [61] is used to compute the exclusion limits.

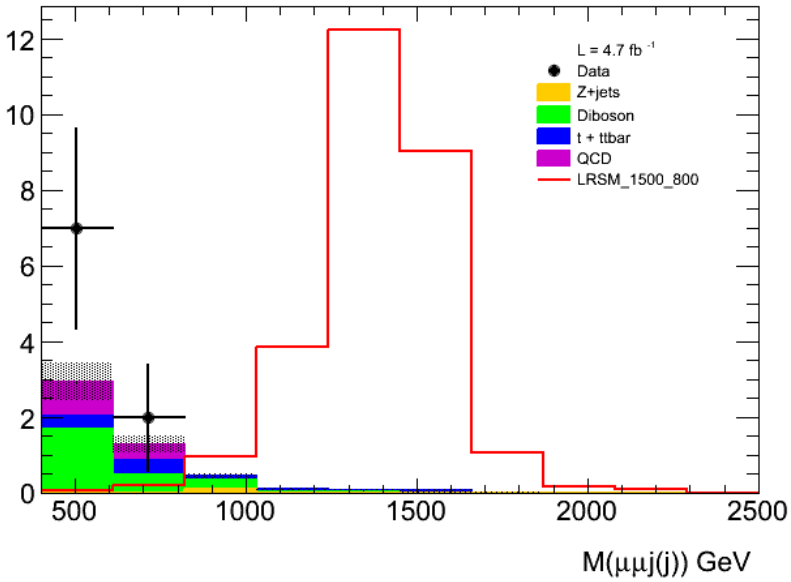

Figure 38: Distributions of $M(\mu\mu j(j))$ is shown for same-sign dimuon events. Additional background suppression criteria $M(\mu\mu) > 110$ GeV and $M(\mu\mu j(j)) > 400$ GeV are applied.

	Events	stat.	Syst.
Z+jets	454.0	21.3	273.2
Dibosons	15.3	3.9	3.4
Top	260.8	16.1	5.3
QCD	144.7	12.0	101.3
Total	874.9	29.5	291.4
Data	654.0		

Table 4: Background estimates for same-sign dimuon pair events and their statistical and systematic uncertainties. Additional background suppression criteria $M(\mu\mu) > 110$ GeV, $M(\mu\mu j(j)) > 400$ GeV and $\sum E_T > 400$ GeV are applied.

	Events	stat.	Syst.
Z+jets	0.1	0.3	0.0
Dibosons	2.4	1.6	0.3
Top	1.1	1.0	0.2
QCD	40.0	6.3	24.0
Total	43.6	6.6	24.0
Data	9.0		

Table 5: Background estimates for same-sign dimuon pair events and their statistical and systematic uncertainties. Additional background suppression criteria $M(\mu\mu) > 110$ GeV and $M(\mu\mu j(j)) > 400$ GeV

RooStats is a project undertaken wit a purpose to create advanced statistical tools required for the analysis of LHC data, with emphasis on discoveries, confidence intervals, and combined measurements. The package RooStats is based on the idea that a standard implementation of all major statistical methods as a set of C++ classes with coherent interfaces would be beneficial for HEP community, so that it can be used with arbitrary models and datasets in a well-defined way allowing to compare and to combine the results of different analyses and even experiments in the simplest possible way.

The method used to calculate the upper limits is based on a Neyman construction [62]. Consider a p.d.f. $f(x;\theta)$ where x represents the outcome (*e.g.*, the observed number of events) of the experiment and θ is an unknown parameter (*e.g.*, the cross section for a BSM process) for which we want to construct a confidence interval. The variable x could (and often does) represent an estimator for θ. Using $f(x;\theta)$, we can determine a pre-specified probability 1α, and for every value of θ, a set of values $x1(\theta,\alpha)$ such that

$$P(x < x_1;\theta) = 1 - \alpha = \int_0^{x_1} f(x;\theta)\, dx \tag{4.1}$$

This is illustrated in Fig. 39. After the probabilities $1-\alpha$ are evaluated, one can determine

the upper limit on the parameter θ for a corresponding outcome x_1, as shown.

Since only the upper limits on cross sections are required, this particular implementation of Neyman construction is one-sided (since we are only interested in the upper limits), as opposed to the more common two-sided implementation. The two-sided implementation can be simply achieved by modifying the Eq. 4.1 as

$$P(x_1 < x < x_2; \theta) = 1 - \alpha = \int_{x_1}^{x_2} f(x; \theta)\ dx \tag{4.2}$$

Such a construction would give a band, instead of a region as shown in Fig. 39.

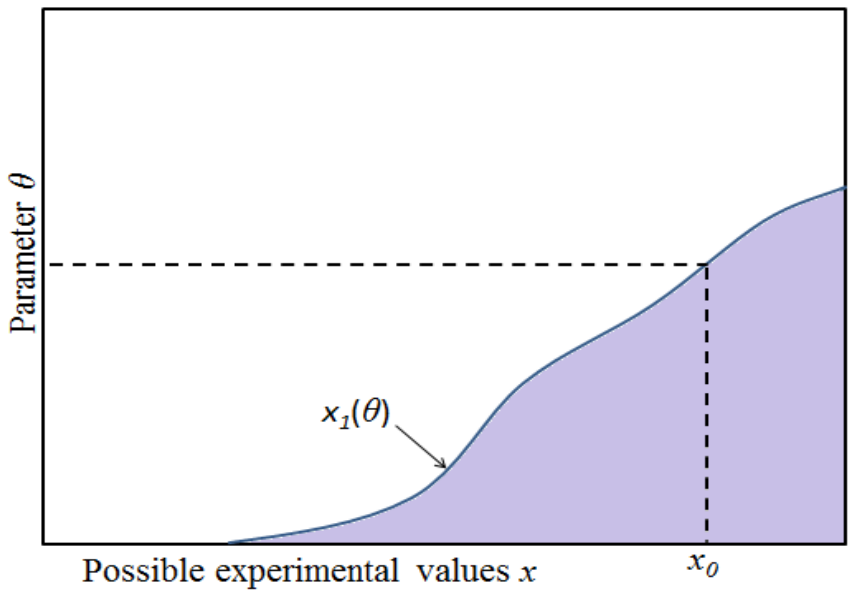

Figure 39: Construction of confidence band.

4.4.1 Systematic Uncertainties for Limit Extraction

Several sources of systematic uncertainties for backgrounds and signal events were considered as described in Chapter 3.1. Shape systematic uncertainties were used for signals and backgrounds, while flat systematic uncertainties of 3.7% on luminosity and 9% on signal acceptance was used.

Exclusion limit plots are shown in Fig. 40 to Fig. 46, for limits obtained for the W_R mass range between 0.6 TeV and 2.3 TeV. The broken line ("theory") shown in the plots

are the cross sections of the signal for the respective mass points. The lines "observed" and "expected" shows the cross-sections excluded at 95% C.L The expected limit is a limit extracted from data assuming that the number of events observed in data is exactly equal to the number of background events. Observed limit is a limit extracted from data using the number of events actually observed. Therefore, if the number of observed events happens to be the same as estimated events the expected and measured limits would be the same. When the theoretical cross section for the signal is larger than the "observed" cross section at some mass point, that theoretical cross section (and the mass) is also excluded because we would have seen the excess in data otherwise. When the theoretical cross section for the signal is less than the "observed" cross section at some mass point, that theoretical cross section is not excluded for the particular set of model parameters used to make that prediction. The uncertainty bands represents the "expected" limits if there were 1σ and 2σ fluctuations in the "expected" background estimations.

Figure 47 shows the summarization of limit setting on masses for W_R and N, in LRSM. SS events give better sensitivity to the signal. While OS channel excludes the $M(W_R)$ up to 1 TeV, the SS channel excludes the $M(W_R)$ up to 1.8 TeV. The masses inside the shaded regions are excluded.

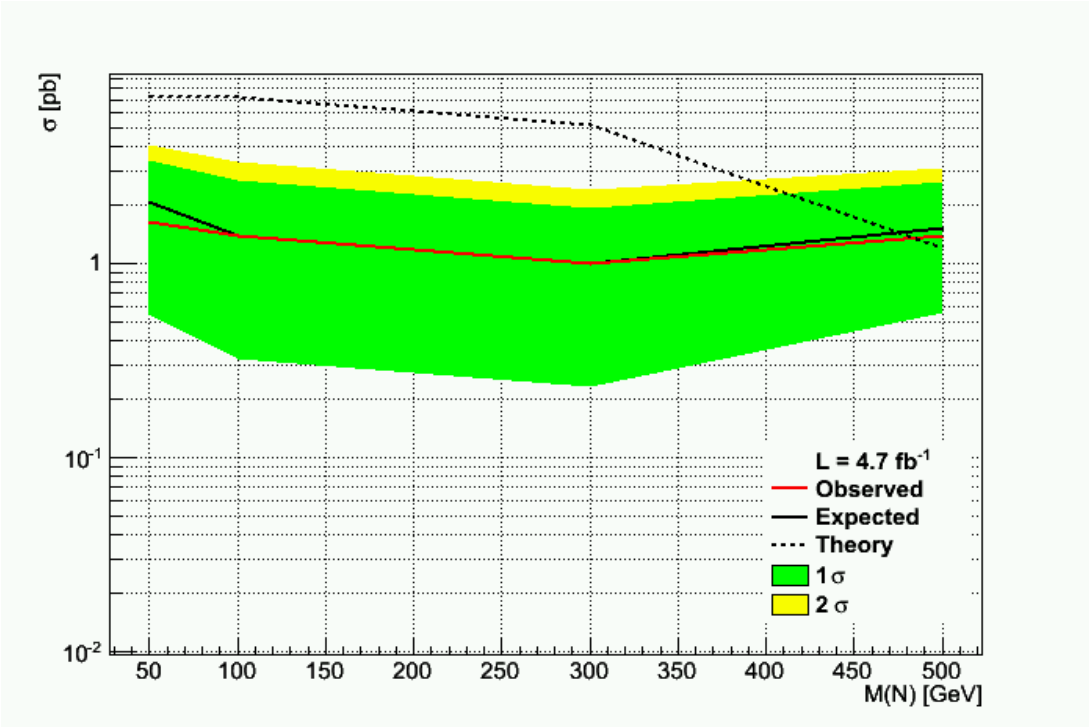

Figure 40: Exclusion limits (at 95% CL) for $M(W_R) = 600$ GeV for opposite-sign (top) $\mu\mu$-jet(s) channels.

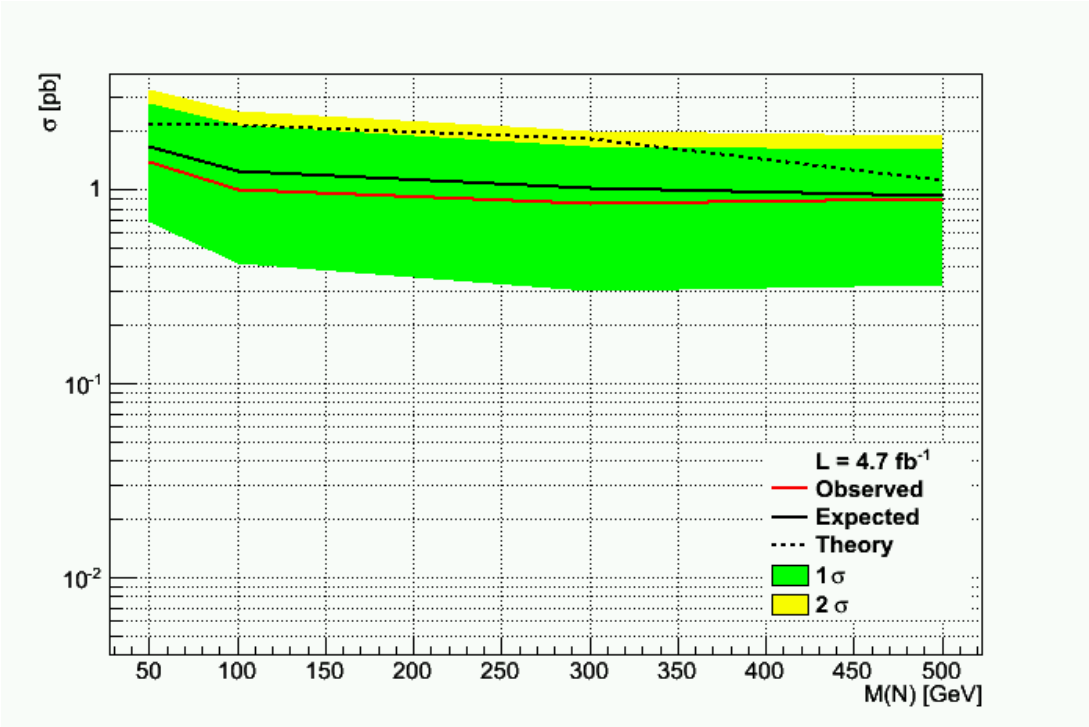

Figure 41: Exclusion limits (at 95% CL) for $M(W_R) = 800$ GeV for opposite-sign (top) $\mu\mu$-jet(s) channels.

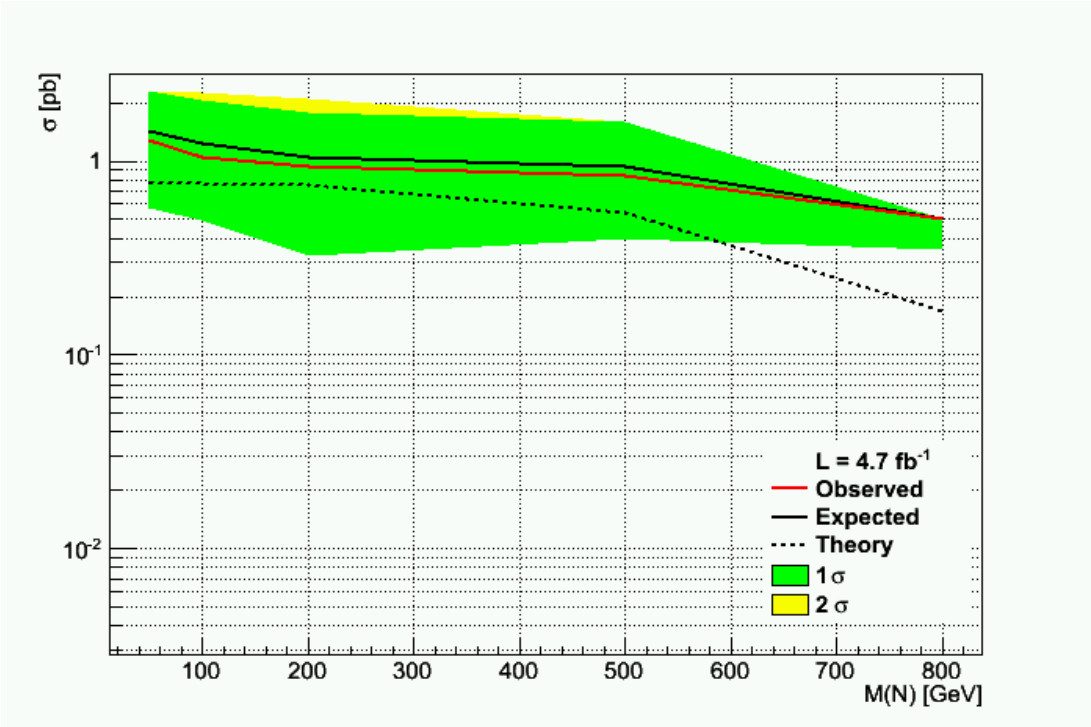

Figure 42: Exclusion limits (at 95% CL) for $M(W_R) = 1000$ GeV for opposite-sign (top) $\mu\mu$-jet(s) channels.

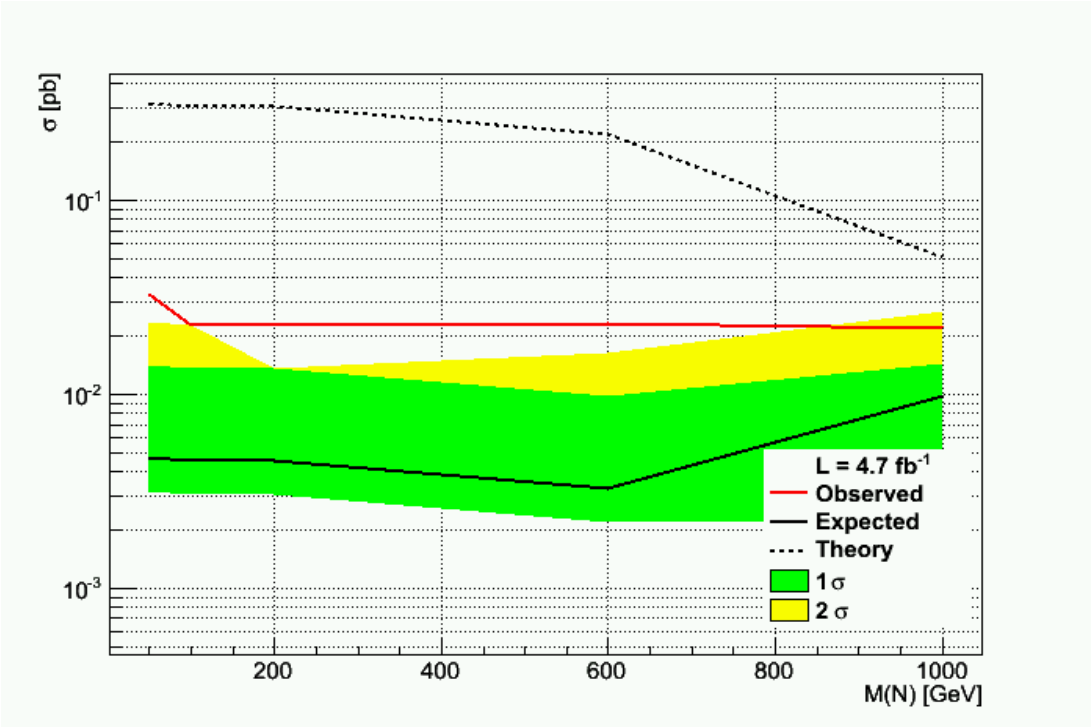

Figure 43: Exclusion limits (at 95% CL) for $M(W_R) = 1200$ GeV for same-sign $\mu\mu$-jet(s) channels.

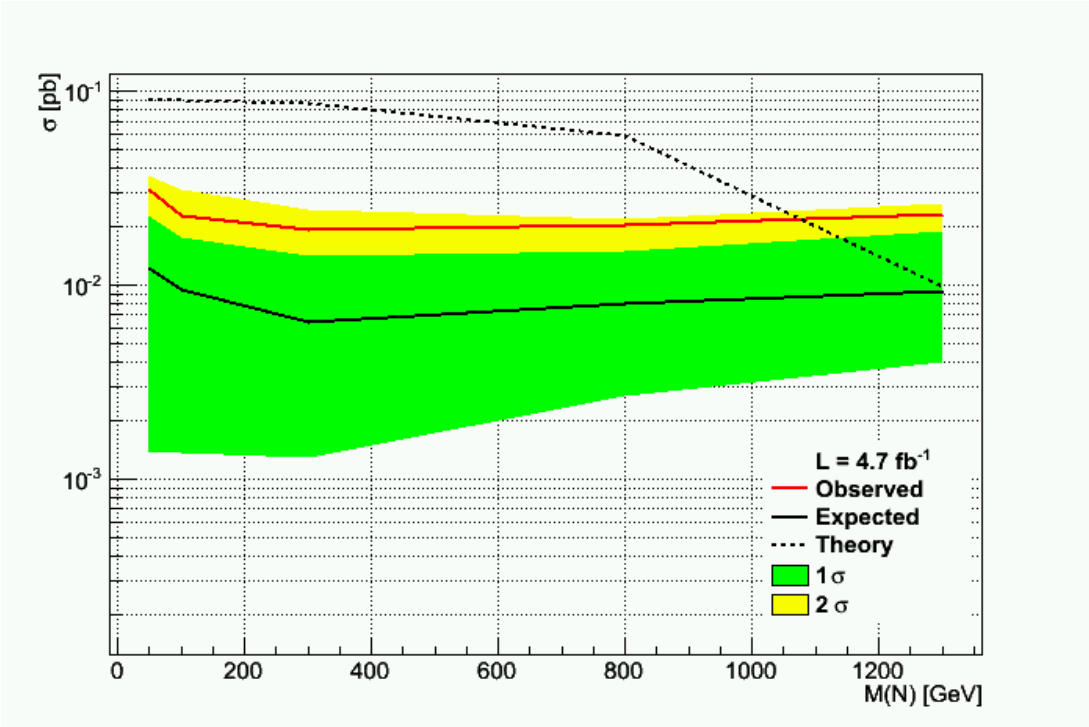

Figure 44: Exclusion limits (at 95% CL) for $M(W_R) = 1500$ GeV for same-sign $\mu\mu$-jet(s) channels.

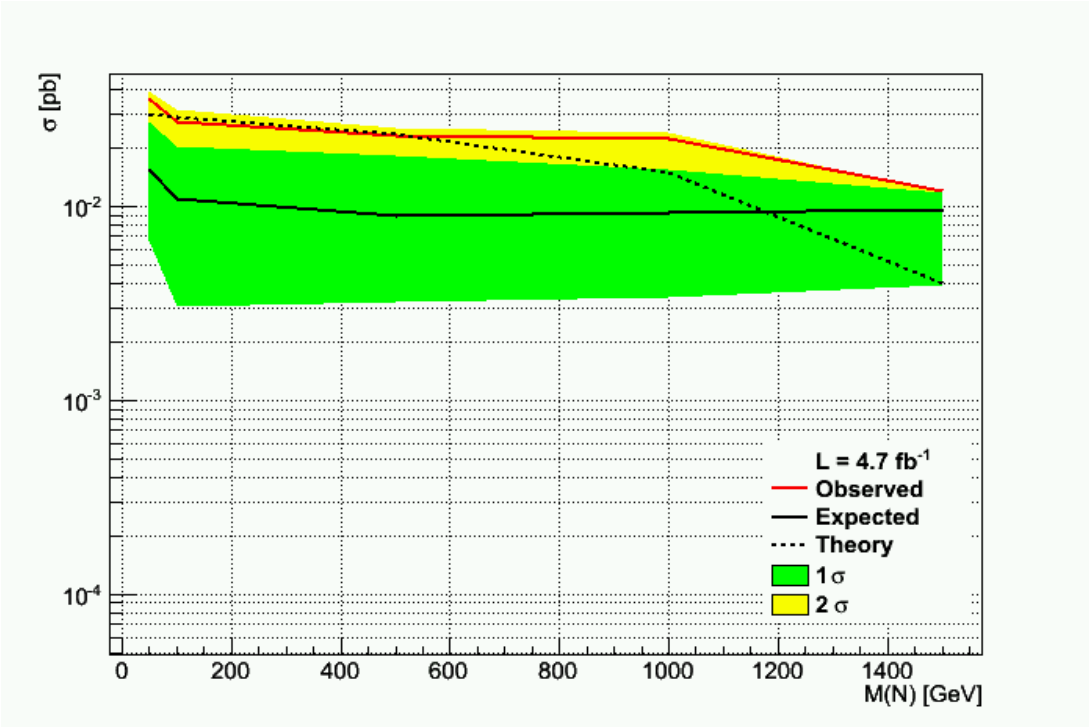

Figure 45: Exclusion limits (at 95% CL) for $M(W_R) = 1800$ GeV for same-sign $\mu\mu$-jet(s) channels.

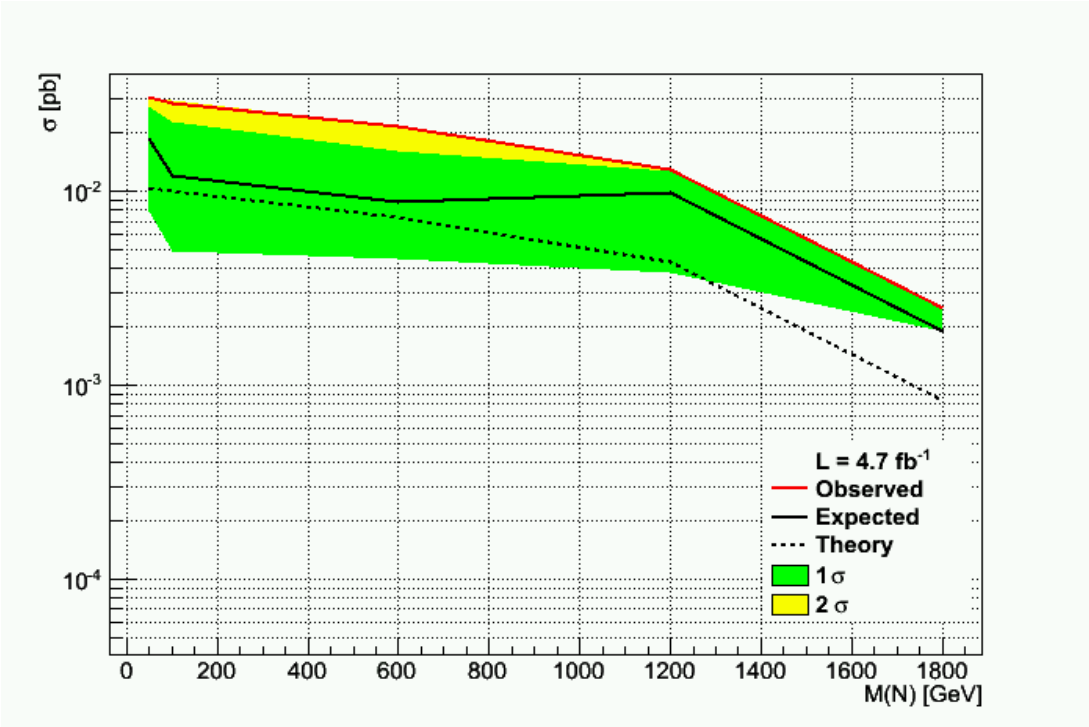

Figure 46: Exclusion limits (at 95% CL) for $M(W_R) = 2100$ GeV for same-sign $\mu\mu$-jet(s) channels.

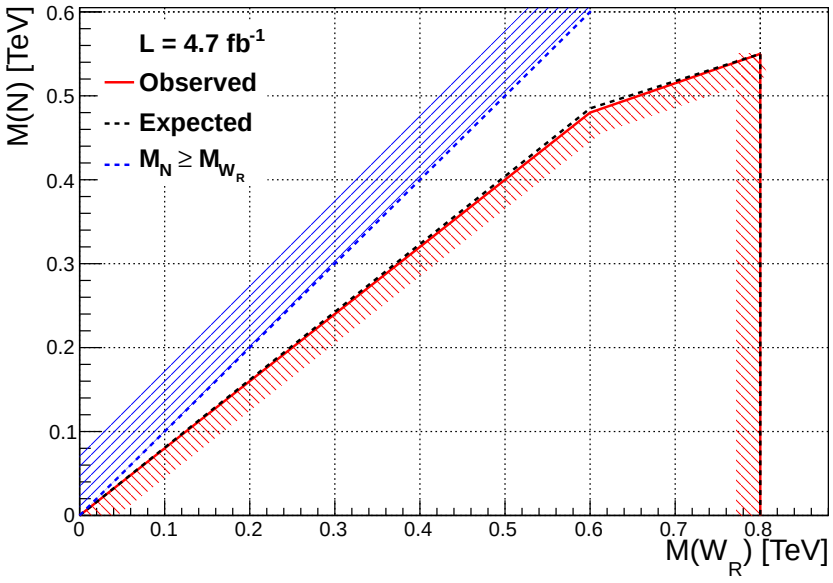

(a)

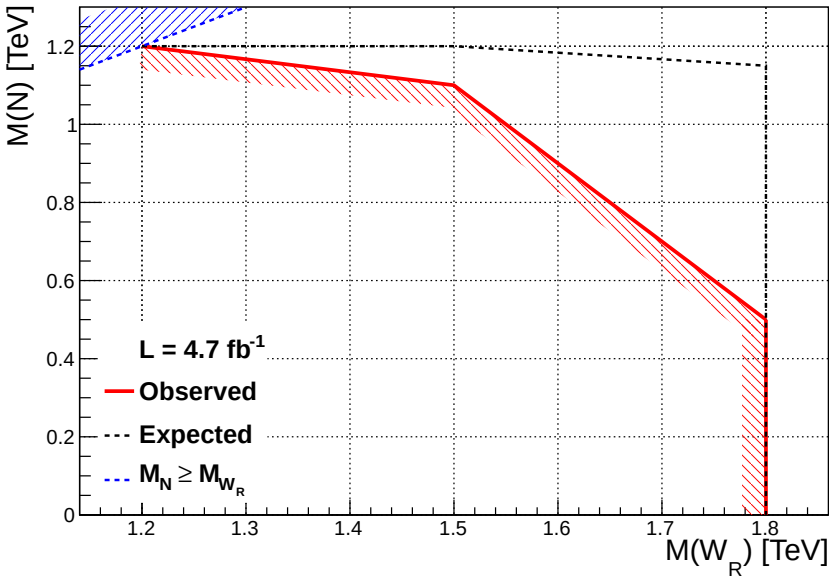

(b)

Figure 47: Exclusion plots for masses of W_R and N at 95% C.L., for OS channel (top) and SS channel (bottom). The shaded regions are excluded. The analysis presented in this thesis is not sensitive to scenarios where the neutrino is heavier than WR (the area above the dashed blue line), because in that case W_R decays primarily into quarks that are hadronized and are detected as jets.

5.0 CONCLUSIONS

A dedicated search for hypothetical heavy neutrinos and W_R bosons in final states with two high p_T same-sign and opposite-sign leptons and hadronic jets has been performed. In a data sample corresponding to an integrated pp luminosity of 4.7 fb^{-1} at $\sqrt{s} = 7$ TeV, no statistically significant deviation from the SM expectations is observed. Mass-dependent 95% C.L. upper limits are set on the products of W_R production cross section and branching fraction for the W_R decay to a heavy neutrino and a charged lepton of the same generation. Lower limits are set on the masses of the hypothetical intermediate vector boson W_R and heavy neutrino N in the framework of a Left-Right Symmetric Model. We exclude a W_R with mass below 1.8 TeV and a heavy neutrino N with mass below 1.2 TeV.

We expect the results presented in this dissertation, obtained and published [26, 27] in the framework of the ATLAS heavy neutrino search group to be soon superceded by our own improved analysis based on the full data sample of 27 fb^{-1}, accumulated at 8 TeV by the ATLAS experiment before the LHC was turned off for an extensive upgrade a few months ago. While the full data analysis is going to push the limits (unless the W_R and heavy neutrinos are discovered) on the W_R mass to above the 3 TeV energy scale, the most interesting results are expected with the future LHC data that will be collected at higher pp center of masses energy of 13−14 TeV. Our estimates based on full MC simulation and the model implemented in *PYTHIA* indicate that after a few years of running the upgraded LHC will be able to probe the W_R and N masses as high as 5 TeV, *i.e.* significantly above the indirect lower limits estimated from the $K_L - K_S$ mass difference and direct searches performed so far. This will be the time for the definitive exploration of the question of possible existence of heavy neutrinos and their connection to the masses of light neutrinos via the seesaw mechanism.

BIBLIOGRAPHY

[1] W. M. Alberico and S. M. Bilenky, *Neutrino Oscillations, Masses and Mixing*, Phys. Part. Nucl. **35**, 297 (2004) [Fiz. Elem. Chast. Atom. Yadra **35**, 545 (2004)].

[2] T. Araki *et al.* [KamLAND Collaboration], *Measurement of Neutrino Oscillation with KamLAND: Evidence of spectral distortion*, Phys. Rev. Lett. **94** 081801 (2005) [hep-ex/0406035].

[3] H. Miyazawa, *Baryon Number Changing Currents*, Prog. Theor. Phys., 36 (6), (1966).

[4] P. Ramond, *Dual Theory for Free Fermions*, Phys. Rev., D3, (1971).

[5] Yu. A. Gol'f and, E. P. Likhtman, *Extension of the Algebra of Poincare Group Generators and Violation of P Invariance*, JETP Lett., **13**, (1971).

[6] J. C. Pati and A. Salam, *Lepton Number as the Fourth Color*, Phys. Rev. D **10**, 275 (1974).

[7] R. N. Mohapatra and J. C. Pati, *A Natural Left-Right Symmetry*, Phys. Rev. D **11**, 2558 (1975).

[8] R. N. Mohapatra and P. B. Pal, *Massive Neutrinos in Physics and Astrophysics. Second edition*, World Sci. Lect. Notes Phys. **60**, 1 (1998) [World Sci. Lect. Notes Phys. **72**, 1 (2004)].

[9] M. Fukugita, T. Yanagida, *Physics of Neutrinos and Applications to Astrophysics*, Springer-Verlag, ISBN 3-540-43800-9 (2003).

[10] A. D. Sakharov, *Violation of CP Invariance, C Asymmetry, and Baryon Asymmetry of the Universe*, JETP 5: 24-27 (1967).

[11] K. Huitu, J. Maalampi, A. Pietila and M. Raidal, *Doubly charged Higgs at LHC*, Nucl. Phys. B **487**, 27 (1997).

[12] A. Ferrari *et al*, *Search for Right-handed Majorana neutrinos at LHC in the ATLAS detector*, Phys. Rev. D **62**, D13001 (2000).

[13] R. N. Mohapatra and G. Senjanovic, *Neutrino Masses and Mixings in Gauge Models with Spontaneous Parity Violation*, Phys. Rev. D **23**, 165 (1981).

[14] R. N. Mohapatra and G. Senjanovic, *Neutrino Mass and Spontaneous Parity Violation*, Phys. Rev. Lett. **44**, 912 (1980).

[15] A. Davidson and K. C. Wali, *Family Mass Hierarchy From Universal Seesaw Mechanism*, Phys. Rev. Lett. **60**, 1813 (1988).

[16] A. Atre, T. Han, S. Pascoli and B. Zhang, *The Search for Heavy Majorana Neutrinos*, JHEP **0905**, 030 (2009).

[17] Z. Maki, M. Nakagawa and S. Sakata, *Remarks on the unified model of elementary particles*, Prog. Theor. Phys. **28**, 870 (1962).

[18] F. R. Klinkhamer and N. S. Manton, *A Saddle Point Solution in the Weinberg-Salam Theory*, Phys. Rev. D **30**, 2212 (1984).

[19] D. Buskulic *et al.* [ALEPH Collaboration], *Search for heavy lepton pair production in e+ e- collisions at center-of-mass energies of 130-GeV and 136-GeV*, Phys. Lett. B **384**, 439 (1996).

[20] P. Abreu *et al.* [DELPHI Collaboration], *Search for composite and exotic fermions at LEP-2*, Eur. Phys. J. C **8**, 41 (1999).

[21] P. Achard *et al.* [L3 Collaboration], *Search for heavy neutral and charged leptons in e^+e^- annihilation at LEP*, Phys. Lett. B **517**, 75 (2001).

[22] G. Abbiendi *et al.* [OPAL Collaboration], *Search for unstable heavy and excited leptons at LEP 2*, Eur. Phys. J. C **14**, 73 (2000).

[23] G. Beall, M. Bander, A. Soni, *Constraint on the Mass Scale of a Left-Right Symmetric Electroweak Theory from the K(L) K(S) Mass Difference*, Phys. Rev. Lett. **48**, 848 (1982).

[24] V. M. Abazov *et al.* [D0 Collaboration], *Search for W' Boson Resonances Decaying to a Top Quark and a Bottom Quark*, Phys. Rev. Lett. **100**, 211803 (2008).

[25] T. Aaltonen *et al.* [CDF Collaboration], *Search for the Production of Narrow t anti-b Resonances in 1.9 fb-1 of p anti-p Collisions at s**(1/2) = 1.96-TeV*, Phys. Rev. Lett. **103**, 041801 (2009).

[26] [ATLAS Collaboration], *A Search for Heavy Majorana Neutrino and WR in dilepton plus jets events with the ATLAS detector in pp collisions at $\sqrt{s}$ = 7 TeV*, ATLAS-CONF-2011-115.

[27] [ATLAS Collaboration], *Search for heavy neutrinos and right-handed W bosons in events with two leptons and jets in pp collisions at $\sqrt{s} = 7$ TeV with the ATLAS detector*, Eur. Phys. J. C **72**, 2056 (2012).

[28] T. S. Pettersson (ed.), P. Lef'evre (ed.), *The Large Hadron Collider : Conceptual Design*, Preprint CERN-AC-95-05 LHC, CERN, (1995).

[29] Y. Baconnier, G. Brianti,P. Lebrun, A. G. Mathewson, R. Perin, *LHC : The Large Hadron Collider Accelerator* Project, Report CERN-AC-93-03-LHC, CERN, (1993).

[30] Press Conference: Update on the search for the Higgs boson at CERN, 4 July 2012 http://indico.cern.ch/conferenceDisplay.py?confId=196564.

[31] [ATLAS Collaboration], *ATLAS Technical Design Report*, ATLAS TDR 14, CERN/LHCC 99-14.

[32] [ATLAS Collaboration], *Expected Performance of ATLAS Experiment*, CERN-OPEN-2008-020.

[33] [ATLAS Collaboration], *Liquid Argon Calorimeter Technical Design Report*, CERN-LHCC-96-041, http://cdsweb.cern.ch/record/331061.

[34] [ATLAS Collaboration], *Tile Calorimeter Technical Design Report*, CERN-LHCC-96-042.

[35] [ATLAS collaboration], *The ATLAS Experiment at the CERN Large Hadron Collider*, JINST 3 S08003 (2008).

[36] T. Sjostrand, S. Mrenna, P. Z. Skands, *PYTHIA 6.4 Physics and Manual*, JHEP **0605**, 026 (2006).

[37] [ATLAS Collaboration], *Charged particle multiplicities in pp interactions at $\sqrt{s} = 0.9$ and 7 TeV in a diffractive limited phase-space measured with the ATLAS detector at the LHC and new PYTHIA6 tune*, ATLAS-CONF-2010-031.

[38] [ATLAS Collaboration], *The ATLAS Simulation Infrastructure*, Eur. Phys. J. **C70**, 823 (2010).

[39] S. Agostinelli et al., *Geant4 - A Simulation Toolkit*, Tech. Rep. NIM **A.506**, (2003).

[40] https://twiki.cern.ch/twiki/bin/view/AtlasPublic/LuminosityPublicResults.

[41] W. -Y. Keung and G. Senjanovic, *Majorana Neutrinos And The Production Of The Right-handed Charged Gauge Boson*, Phys. Rev. Lett. **50**, 1427 (1983).

[42] R. N. Mohapatra and R. E. Marshak, *Local B-L Symmetry of Electroweak Interactions, Majorana Neutrinos and Neutron Oscillations*, Phys. Rev. Lett. **44**, 1316 (1980) [Erratum-ibid. **44**, 1643 (1980)].

[43] J. Collot and A. Ferrari, *Search for right-handed Majorana neutrinos at LHC in the ATLAS detector*, ATL-PHYS-98-124.

[44] A. Ferrari, J. Collot, M-L. Andrieux, B. Belhorma, P. de Saintignon, J-Y. Hostachy, P. Martin and M. Wielers, *Sensitivity study for new gauge bosons and right-handed Majorana neutrinos in pp collisions at* $\sqrt{s}$ *= 14-TeV*, Phys. Rev. D **62**, 013001 (2000).

[45] M. Cacciari, G. P. Salam and G. Soyez, *The anti-kt jet clustering algorithm*, JHEP 0804 063 (2008).

[46] https://twiki.cern.ch/twiki/bin/viewauth/ AtlasProtected/MCPAnalysisGuidelinesRel17MC11a.

[47] [ATLAS Collaboration], *Muon Momentum Resolution in First Pass Reconstruction of pp Collision Data Recorded by ATLAS in 2010*, ATLAS-CONF-2011-046.

[48] [ATLAS Collaboration], *Muon reconstruction efficiency in reprocessed 2010 LHC proton-proton collision data recorded with the ATLAS detector*, ATLAS-CONF-2011-063.

[49] M. R. Whalley, D. Bourilkov and R. C. Group, *The Les Houches accord PDFs (LHAPDF) and LHAGLUE*, arXiv:0508110 [hep-ph].

[50] A. Sherstnev and R. S. Thorne, *Parton Distributions for LO Generators*, Eur. Phys. J. C **55**, 553 (2008).

[51] M. Botje *et al.*, *The PDF4LHC Working Group Interim Recommendations* arXiv:1101.0538 [hep-ph].

[52] J. Alwall *et al.*, *MadGraph/MadEvent v4: The New Web Generation*, JHEP **0709**, 028 (2007).

[53] S. Frixione and B. R. Webber, *Matching NLO QCD computations and parton shower simulations*, JHEP **0206**, 029 (2002).

[54] S. Frixione, P. Nason and B. R. Webber, *Matching NLO QCD and parton showers in heavy flavor production*, JHEP **0308**, 007 (2003).

[55] G. Marchesini, B. R. Webber, G. Abbiendi, I. G. Knowles, M. H. Seymour and L. Stanco, *HERWIG: A Monte Carlo event generator for simulating hadron emission reactions with interfering gluons. Version 5.1 - April 1991*, Comput. Phys. Commun. **67**, 465 (1992).

[56] http://lhc-commissioning.web.cern.ch/lhc-commissioning/.

[57] [ATLAS Collaboration], *Jet energy scale and its systematic uncertainty in ATLAS for jets produced in proton-proton collisions at* $\sqrt{s} = 7\ TeV$ *in ATLAS 2010 data*, ATLAS-CONF-2011-032.

[58] [ATLAS Collaboration], *Luminosity Determination in pp Collisions at* $\sqrt{(s)} = 7\ TeV$ *using the ATLAS Detector in 2011*, ATLAS-CONF-2011-116.

[59] [ATLAS Collaboration], *Jet Energy Resolution from In-situ Techniques with the ATLAS Detector Using Proton-Proton Collisions at a Center of Mass Energy* $\sqrt{s} = 7\ TeV$, ATL-COM-PHYS-2011-240.

[60] [ATLAS Collaboration], *Close-by Jet Effects on Jet Energy Scale Calibration in pp Collisions at* $\sqrt{(s)} = 7\ TeV$ *with the ATLAS Detector*, ATLAS-CONF-2011-062.

[61] L. Moneta *et al.*, *The RooStats Project*, PoS ACAT **2010**, 057 (2010).

[62] J. Neyman, *Outline of a Theory of Statistical Estimation Based on the Classical Theory of Probability*, Phil. Trans. R. Soc. Lond. A vol. 236 no. 767 333-380 (1937).

[63] S. Chatrchyan *et al.* [CMS Collaboration], *Search for heavy neutrinos and W[R] bosons with right-handed couplings in a left-right symmetric model in pp collisions at sqrt(s) = 7 TeV*, Phys. Rev. Lett. **109**, 261802 (2012).